

The Global Climate and Atmospheric Dynamics of Extrasolar Lava Planets



Mark Hammond
Hertford College
University of Oxford

A thesis submitted for the degree of
Doctor of Philosophy
Michaelmas Term 2019

Dedicated to whomever

Acknowledgements

Lorem ipsum dolor sit amet, consectetuer adipiscing elit. Ut purus elit, vestibulum ut, placerat ac, adipiscing vitae, felis. Curabitur dictum gravida mauris. Nam arcu libero, nonummy eget, consectetuer id, vulputate a, magna. Donec vehicula augue eu neque. Pellentesque habitant morbi tristique senectus et netus et malesuada fames ac turpis egestas. Mauris ut leo. Cras viverra metus rhoncus sem. Nulla et lectus vestibulum urna fringilla ultrices. Phasellus eu tellus sit amet tortor gravida placerat. Integer sapien est, iaculis in, pretium quis, viverra ac, nunc. Praesent eget sem vel leo ultrices bibendum. Aenean faucibus. Morbi dolor nulla, malesuada eu, pulvinar at, mollis ac, nulla. Curabitur auctor semper nulla. Donec varius orci eget risus. Duis nibh mi, congue eu, accumsan eleifend, sagittis quis, diam. Duis eget orci sit amet orci dignissim rutrum.

Abstract

This thesis aims to understand the global circulation of tidally locked lava planets, and how to interpret observations of them.

Contents

1	Introduction	1
2	Tidally Locked Lava Planets and 55 Cancri e	6
2.1	Exoplanets	7
2.2	Lava Planets	9
2.2.1	Tidally Locked Planets	9
2.2.2	The Atmospheric Circulation of Tidally Locked Planets	10
2.2.3	Lava Planets	10
2.3	55 Cancri e	10
3	Wave-Mean Flow Interactions in a Linear Theory of Tidally Locked Atmospheres	12
3.1	The Shallow-Water Equations	15
3.1.1	Free Solutions	16
3.1.2	Forced Solutions	17
3.1.3	Wave Interactions with Flow	20
3.2	Zonal Acceleration	21
3.2.1	Acceleration in a Matsuno-Gill Model	21
3.2.2	Correction to Vertical Momentum Transport	23
3.2.3	Equilibrium Equatorial Flow	25
3.2.4	Horizontal Momentum Transport from Stationary Waves	26
3.2.5	Horizontal Momentum Transport from Transient Waves	26
3.3	Wave Interactions with Shear Flow on the Beta-Plane	26
3.3.1	Free Modes	30
3.3.2	Forced Solutions	33
3.3.3	Equilibrium Circulation	33
3.3.4	Damping	34

3.3.5	Hot-Spot Shift	34
3.4	Wave Interactions with Shear Flow on a Sphere	35
3.4.1	Spherical Shallow-Water Equations	35
3.4.2	Forced Solutions	35
3.5	Scaling Relations	35
3.5.1	1D Scaling Relations	35
3.5.2	2D Scaling Relations	35
3.6	Other Jet Patterns	35
4	Non-Linear Tests of a Linear Theory of Tidally Locked Atmospheres	36
4.1	Non-Linear Tests of Linear Shallow-Water Theory	37
4.2	GCM Tests of Shallow-Water Theory	44
5	Equilibrium Circulation States on Tidally Locked Planets	45
5.1	Equilibrium Flow Profile	45
5.2	Initial Conditions	47
5.3	Instabilities as deviations from equilibrium	47
5.4	Jet Scaling Relations	47
6	Linking the Climate and Thermal Phase Curve of 55 Cancri e	48
6.1	Observations of 55 Cancri e	50
6.2	Simulating a Lava Planet	55
6.3	Simplified Scaling Theory	55
6.4	Idealised Simulations	56
6.4.1	Mean Molecular Weight	56
6.4.2	Surface Pressure	56
6.4.3	Optical Thickness	56
6.4.4	Vertical Structure	56
6.4.5	Phase Curves	56
6.5	Discussion	56
7	Clouds on Lava Planets	57
7.1	Clouds on Lava Planets	58
7.2	Simulations of Clouds	58
7.3	Effect on Observations	58
8	Introduction	59

9 Conclusions	64
Bibliography	65
A Exo-FMS	67
A.1 Model Structure	68
A.2 Dynamics	68
A.3 Radiative Transfer	69
A.4 Cloud Microphysics	69
B GFDL-SDC	70
C Pseudo-Spectral Methods	71
C.1 Solving Equations	72
C.2 Example Solutions	75

List of Figures

1.1	The population of known exoplanets plotted by semi-major axis and stellar mass. All the planets below the line have a timescale to reach a tidally locked state of less than 0.1 billion years, so are expected to be in this state.	3
3.1	Example GCM results.	13
3.2	Free Modes.	17
3.3	Forced solutions.	19
3.4	Acceleration terms.	22
3.5	Acceleration terms with R.	24
3.6	Eigenvalue shift.	29
3.7	The meridional structure of the free Kelvin mode.	29
3.8	The meridional structure of the free Rossby mode (Hammond and Pierrehumbert, 2018).	30
3.9	Zero Flow and Shear Flow.	34
4.1	The linear response.	38
4.2	5e3.	40
4.3	Nonlinear.	40
4.4	Matsuno jet control.	41
4.5	Nonlinear with and without imposed jet.	42
6.1	Phase curve.	51

List of Figures

6.2	Temperature map.	52
8.1	The population of known exoplanets plotted by semi-major axis and stellar mass. All the planets below the line have a timescale to reach a tidally locked state of less than 0.1 billion years, so are expected to be in this state.	61
C.1	Basis functions used in beta-plane and spherical coordinates.	75
C.2	Coefficients of the pseudo-spectral solution on the beta-plane coordinates with and without a background jet (the plots in Figure ??). The method identifies the exact solution in the first case, and converges rapidly to an accurate solution in the second case.	77
C.3	Coefficients of the pseudo-spectral solution in spherical coordinates (the first plot in Figure ??), with the height variable h and the rescaled height γ . Rescaling the height makes the method converge to a smooth solution at the poles. . .	78

CHAPTER 1

Introduction

“Any finite number divided by infinity is as near to nothing as makes no odds, so the average population of all the planets in the Universe can be said to be zero. From this it follows that the population of the whole Universe is also zero, and that any people you may meet from time to time are merely the products of a deranged imagination.”

— Douglas Adams, *The Restaurant at the End of the Universe*

Lava planets are rocky, very hot, and orbit so close to their host stars that they are expected to be tidally locked to them. This means that they always present the same side to the star, so have a permanent day-side and night-side. This thesis investigates the question of what these properties mean for the atmosphere of the planet, particularly its circulation and composition. Tidally locked planets are very common and observable. Lava planets are particularly observable, especially for rocky planets.

Why are tidally locked planets important? Their unusual situation could make them seem like oddities, unrelated to the majority of planets. On the contrary, Figure 8.1 shows that a large fraction of known exoplanets are expected to be tidally locked. It shows the stellar masses and semi-major axes for all exoplanets listed on the NASA Exoplanet Archive

at the time of writing, with all the planets below the line expected to be tidally locked
([Pierrehumbert and Hammond, 2018](#)).

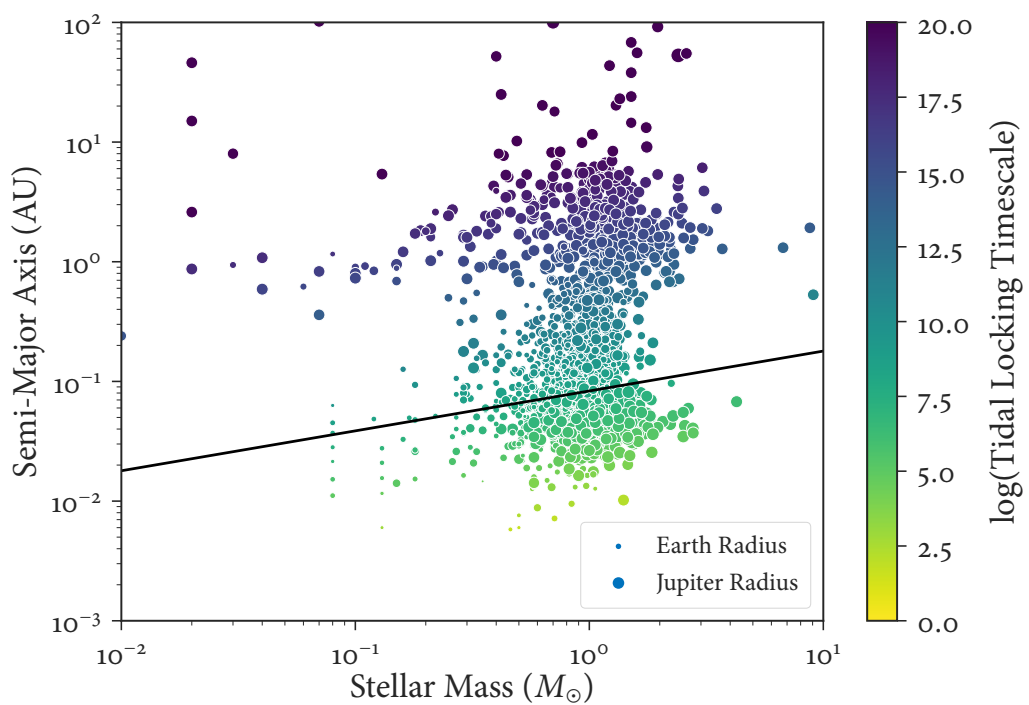


Figure 1.1: The population of known exoplanets plotted by semi-major axis and stellar mass. All the planets below the line have a timescale to reach a tidally locked state of less than 0.1 billion years, so are expected to be in this state.

These planets are also generally more easily characterised than the others, giving larger signals for spectroscopy when they transit their stars. This tendency may have created a detection bias, where close-in exoplanets are more likely to be detected so it appears that a greater fraction are tidally locked than is actually the case. Even if this is true, it does not detract from the relevance of tidally locked planets – we can only study planets we know about!

In Chapter 1, I discuss the concept of a “lava planet” and review the literature of discovery, characterisation, and modelling of such planets. I aim to introduce the scientific concepts and questions that I will address through the rest of the thesis.

In Chapter 2, I discuss the theoretical work I did to understand the global circulation of tidally locked planets in general. In the course of trying to understand simulations of tidally locked lava planets, we found that there was not a full understanding of key features of their circulation. I explain how I used a two-dimensional model to represent the atmosphere of a tidally locked planet, and demonstrated that the equatorial jet that forms affects the global circulation and temperature pattern. This was key to our work on lava planets, but was applicable to any tidally locked planet.

Chapter 3 follows Chapter 2

In Chapter 3, I introduce the model I used to simulate three-dimensional planetary atmospheres, the General Circulation Model (GCM) Exo-FMS. Developing this model formed a large part of the work of my DPhil. I discuss the structure I developed, and the physical processes represented within it. I focus on the particular challenges of simulating tidally locked lava planets, and defer many technical details to Appendix A.

In Chapter 4, I discuss my first project using the simulations discussed in Chapter 3, to

interpret observations of a lava planet.

Chapter 5 follows Chapter 4, and shows how in collaboration with Graham Lee we simulated dynamic, radiatively active clouds on 55 Cancri e in order to answer the questions raised by Chapter 4 on the effect of clouds in its atmosphere.

In the Conclusion, I summarise my work on the global circulation of tidally locked planets, and its relevance for 55 Cancri e.

CHAPTER 2

Tidally Locked Lava Planets and 55 Cancri e

“One face is forever sunlit, and one forever dark, and only the planet’s slow liberation gives the twilight zone a semblance of seasons.”

— Stanley G. Weinbaum, *The Lotus Eaters*

Perhaps the most exciting discovery from the field of exoplanet science is that other stars host planets which are very different from those in our solar system. There are similar planets to those in the solar system – “Hot Jupiters”, high-temperature Jupiter-sized gas giants in short-period orbits, or “Mini-Neptunes”, which show the literal-mindedness of planetary scientists. But some exoplanets have no analogues in the solar system, and “lava planets” are some of the best examples of these.

This short chapter describes the class of “lava planets”, particularly the planet 55 Cancri e, and discusses the question that this thesis aims to answers about this planet.

I will describe lava planets in general, and list the known planets in this class. I will then discuss the 55 Cancri system, and the lava planet 55 Cancri e in that system.

I will try to show that lava planets are a potentially bountiful area for scientific work, being interesting systems that have observational advantages. I will set up the question of the atmosphere and atmospheric circulation of 55 Cancri e, and show how it relates to the broader question of the nature of the climate of tidally locked planets.

2.1 Exoplanets

Exoplanets are planets orbiting stars other than our Sun. As far as we know, there is nothing fundamental to distinguish the planets in our Solar System from those elsewhere, so it is possible that this specific nomenclature may eventually disappear. I will use the word “exoplanet” when discussing specific planets or issues related to their distance, and “planet” in a more general or idealised context (such as the first sentence of this paragraph).

There is no better way to date a piece of writing on exoplanets than by announcing how many have been discovered, so I will just note that we know of several thousand and anticipate many more to come. The number of exoplanets which are favourable for detailed observations is still quite small, and we can observe atmospheric details for perhaps only a few dozen planets. In fact, while the title of this thesis suggests it looks at “lava planets”, there is really only one that is currently observable – 55 Cancri e. Despite this, I hope to draw general conclusions about the circulation of many types of planet, and contribute to an understanding of tidally locked planets and lava planets for future observations.

Discovering Exoplanets

This is not a thesis on discovering exoplanets, although the methods of discovery are sometimes relevant to the characterisation that is of interest. Most exoplanets discovered to date have been found using either a “radial velocity” method or a “transit” method.

In the first method, the motion of a star around its common center of mass with a planet orbiting it is detected by measuring the Doppler-shift of emission lines of the star. The magnitude and period of this motion gives the period of the planet’s orbit, and a limit on its mass.

In the second method, a planet passing across the line of sight from an observer to the star produces a dip in the light seen by the observer. A periodic dip gives the period of the planet, and the size of the dip gives its radius. So, if a planet can be measured with both methods the observer retrieves its period, mass, radius, density, semi-major axis, and equilibrium temperature.

Characterising Exoplanets

This is also not a thesis on characterising exoplanets, although I have tried to keep observations in mind throughout the simulations and theory.

The atmospheres of exoplanets can be characterised through transmission and emission spectroscopy. In transmission spectroscopy, light from the host star passes through the atmosphere of the exoplanet before it reaches the observer, and the spectrum is measured. An alternative (but equivalent) view is that the planet appears to have a different radius as it transits its star at different wavelengths – at a wavelength the atmosphere is

more opaque to, the planet appears larger – so the absorption spectrum of the gases in the atmosphere can be retrieved.

In emission spectroscopy, the spectrum of the light emitted thermally by the planet and its atmosphere is measured. Hotter planets emit more light in this way, so are better suited to this method.

2.2 Lava Planets

2.2.1 Tidally Locked Planets

A tidally locked planet, or a “synchronously rotating” planet, always presents the same face to the star it orbits, as its rotation period is the same as its orbital period. An asynchronously rotating planet like the Earth has a different rotation period (1 day) to its orbital period (1 year). Tidal forces slow down the rotation of such planets, until they become tidally locked. The time for a planet to become tidally locked is approximately:

See Chapter 3 for an investigation of the atmospheric dynamics of tidally locked planets.

Tidally locked planets include Hot Jupiters, Earth-like planets like those in the Trappist-1 system, and lava planets like 55 Cancri e, discussed next.

2.2.2 The Atmospheric Circulation of Tidally Locked Planets

2.2.3 Lava Planets

“Lava Planets” are terrestrial (rocky, not gaseous) planets orbiting very close to their parent star.

2.3 55 Cancri e

55 Cancri e is a tidally locked lava planet orbiting the binary star 55 Cancri, 41 light years away in the constellation of Cancer.

The 55 Cancri system

Figure X shows the 55 Cancri system.

55 Cancri e

55 Cancri e is the closest planet to the G-star 55 Cancri A.

A Thermal Phase Curve of 55 Cancri e

A phase curve is the light measured from a planet as it orbits its star. They are particularly useful for tidally locked planets. Figure X shows a phase curve for X.

A thermal phase curve refers to the light emitted by the planet itself, rather than the light it reflects from the star it orbits. For a tidally locked planet, the thermal phase curve

shows the hemisphere-averaged brightness temperature of the planet as it rotates.

[Demory et al. \(2016\)](#) measured a thermal phase curve of the planet 55 Cancri e.

55 Cancri e is currently the most easily observable terrestrial tidally locked planet. Its composition, atmosphere, and circulation provide tests of theories of planet formation and atmospheric dynamics. In this thesis, I will use it as a case study for the atmospheric dynamics of tidally locked planets.

CHAPTER 3

Wave-Mean Flow Interactions in a Linear Theory of Tidally Locked Atmospheres

“One might as well approximate the derivatives well instead of badly”

— John P. Boyd, *Chebyshev and Fourier Spectral Methods*

Tidally locked planetary atmospheres have such a different spatial energy input to planets like the Earth that it is not obvious that conventional Earth-like atmospheric dynamics should be able to describe them. However, the planetary-scale day-night forcing difference makes the global circulation highly susceptible to a simple shallow-water model, compared to the higher order effects controlling the Earth’s atmosphere.

This chapter discusses my work using a single-layer linear shallow-water model to investigate the global circulation of tidally locked planets. It follows directly from the work of XX and XX. As introduced in Chapter 2, the atmospheres of tidally locked planets are understood to generally have a strong eastward equatorial jet, a hot-spot shifted eastward of their substellar point, and a pair of cold low-pressure lobes on their night-side. Figure 3.1 shows a GCM simulation of a tidally locked planet with Earth-like size and instellation,

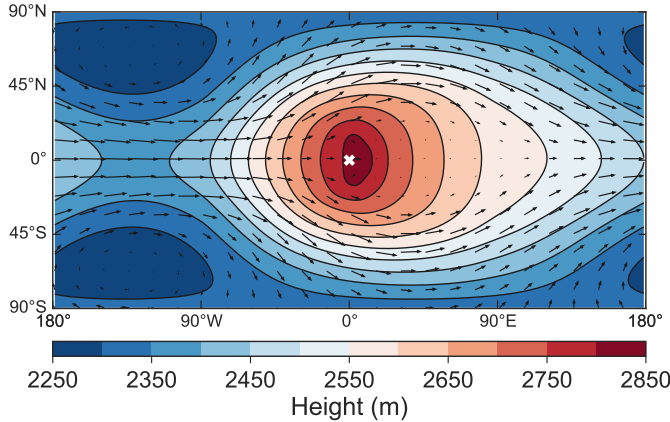


Figure 3.1: Example GCM results.

showing these features.

In this chapter, I will show that the interaction of this mean zonal flow and the standing waves produced by the stationary day-night forcing is crucial to the global circulation of tidally locked planets. [Showman and Polvani \(2011\)](#) used a shallow-water model to model the standing waves on tidally locked planets, and to explain the equatorial superrotation. However, the equilibrium state of their shallow-water model only matched the form of their GCM simulations over the first few days after spin-up from rest. [Tsai et al. \(2014\)](#) suggested that this was because the zonal flow shifted the standing wave response eastwards, and used a uniform flow (with no height perturbation) in a shallow-water model to show this. In this chapter, I follow both of these studies and linearise the shallow-water equations around a meridionally sheared zonal flow $\bar{U}(y)$ with an associated height perturbation $\bar{H}(y)$. I show that the response to day-night forcing in this system matches GCM simulations of tidally locked planets, particularly the form of the hot-spot shift and the cold

lobes on the night-side.

After introducing the linear shallow-water model and the work of Matsuno, Gill, Showman, and Tsai, I will show how I linearised the model about a zonally uniform jet $\bar{U}(y)$ with latitudinal shear, as well as its associated geostrophic height perturbation $\bar{H}(y)$

In Section 1, I will introduce the system of shallow-water equations on a rotating beta-plane, and discuss the response to a day-night forcing, in zero background flow and in uniform background flow (an approximation to the later shear flow and height perturbation).

In Section 2, I will show the zonal acceleration produced by this forced response, discussing how [Showman and Polvani \(2010\)](#) showed that a correction to the classical model of [Matsuno \(1966\)](#) is required to produce equatorial superrotation.

In Section 3, I will linearise the beta-plane shallow-water equations about a background flow $\bar{U}(y)$ and associated height perturbation $\bar{H}(y)$, representing the flow produced by this acceleration. I will find the free modes of this system and the response to the same day-night forcing as before. This will show that the forced response is shifted eastwards, combining with the zonally uniform jet perturbation to produce the global circulation pattern seen in GCM simulation and hinted at by observations.

In Section 4, I will show the same calculation for the shallow-water equations on a sphere, which have less intuitive solutions but are more directly comparable to real planets and GCM simulations.

In Section 5, I will use the shallow-water equations to produce simple one-dimensional scaling relations for the height field along the equator, and compare them to the two-dimensional scaling relations predicted by the solutions in the previous sections.

In the next chapters, I will return to these stationary solutions and scaling relations to compare them to GCM simulations.

I will show that linearising the jet about the shear flow and its height perturbation makes the forced linear response match nonlinear GCM simulations much more closely. The new model reveals scaling relations between the planetary parameters such as forcing strength, and the observable quantities such as the eastward hot-spot shift.

This chapter is based on work produced for [Hammond and Pierrehumbert \(2018\)](#). Some of the figures, which I generated, have been taken directly from this paper. None of the text has been reused, and the structure is significantly different.

3.1 The Shallow-Water Equations

We used the linear shallow-water equations on a one-layer equatorial beta-plane to model the atmosphere of a tidally locked planet. These equations describe the motion of a single layer of fluid of constant density where the horizontal scale of its flow is much greater than the depth of the fluid. The linear form of these equations describe small perturbations to this layer ([Vallis, 2006](#)). We model the atmosphere of a tidally locked planet with a similar shallow-water model to [Showman and Polvani \(2011\)](#). The model corresponds to an active upper layer following the single-layer shallow water equations, above a quiescent layer which can transport mass and momentum to and from the upper layer. The forcing due to stellar heating is represented by Q , a relaxation to the radiative equilibrium height field.

3.1.1 Free Solutions

In this section, we derive the wave response to stationary forcing on the beta-plane ([Matsuno, 1966](#)). The beta-plane system approximates the Coriolis parameter as linear, which is only accurate at low latitudes but leads to more intuitive and useful solutions than the full spherical geometry. We solve the equations in a spherical geometry in Section ??, and show that the beta-plane approximation leads to very similar solutions, as in other studies of the atmospheres of tidally locked planets ([Showman and Polvani, 2011](#)) ([Heng and Workman, 2014](#)).

All the quantities are linearized as the sum of a zonally mean background value $F(y)$ and a perturbation with the form $f(y)e^{i(k_x x - \omega t)}$ (unlike [Matsuno \(1966\)](#), who uses the less conventional form $f(y)e^{i(k_x x + \omega t)}$). Throughout this paper, we will use capital letters for mean zonal quantities such as \bar{U} and \bar{H} , and lower-case letters for perturbations to this background, such as u and h (unless otherwise specified, such as the forcing Q). The shallow-water equations for these perturbations with zero background flow are:

$$\begin{aligned} \frac{\partial u}{\partial t} - \beta y v + \frac{\partial h}{\partial x} &= 0 \\ \frac{\partial v}{\partial t} + \beta y u + \frac{\partial h}{\partial y} &= 0 \\ \frac{\partial h}{\partial t} + c^2 \left(\frac{\partial u}{\partial x} + \frac{\partial v}{\partial y} \right) &= Q(x, y) \end{aligned} \quad (3.1)$$

where h is the height, $c = \sqrt{gH}$ is the gravity wave speed ([Matsuno, 1966](#)), and there is no friction or damping. Non-dimensionalizing with time scale $\sqrt{1/c\beta}$ and length scale $\sqrt{c/\beta}$ (the equatorial Rossby radius of deformation L_R), and assuming all quantities have the form $f(y)e^{i(kx - \omega t)}$, the free equations with zero forcing are:

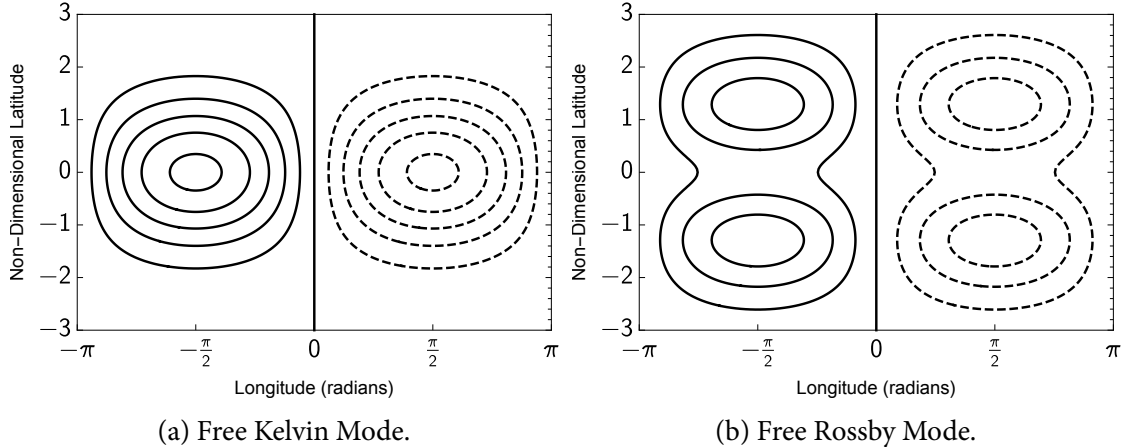


Figure 3.2: Free Modes.

$$\begin{aligned}
 -i\omega u - yv + ik_x h &= 0 \\
 -i\omega v + yu + \frac{\partial h}{\partial y} &= 0 \\
 -i\omega h + iku + \frac{\partial v}{\partial y} &= 0
 \end{aligned} \tag{3.2}$$

Matsuno (1966) gives the free modes of this system as XX. Figure 3.2a shows the free Kelvin mode with wavenumber 1 and Figure 3.2b shows the free Rossby mode with wavenumber 1.

EIGENVALUES GIVE POSITION IN FORCED RESPONSE.

3.1.2 Forced Solutions

In this chapter, I will focus on the response of the shallow-water equations to a forcing $Q(x, y)$ on the height field h , representing the stellar forcing on a tidally locked planet. The forced solution can be considered to be a sum of the free modes discussed in the previous

section, at different locations and with different strengths.

The forced equations are:

$$\begin{aligned}\alpha_{rad}u - \beta yv + \frac{\partial h}{\partial x} &= 0 \\ \alpha_{rad}u + \beta yu + \frac{\partial h}{\partial y} &= 0 \\ \alpha_{dyn}h + c^2\left(\frac{\partial u}{\partial x} + \frac{\partial v}{\partial y}\right) &= Q(x, y)\end{aligned}\quad (3.3)$$

with boundary conditions

$$u, v, h \rightarrow 0 \quad \text{for } y \rightarrow \pm\infty. \quad (3.4)$$

Matsuno (1966) shows how the response of Equation 3.3 to a forcing $Q(x, y) = Q_0 \sin(x) e^{-y^2/2}$ and uniform damping $\alpha_{rad} = \alpha_{dyn} = \alpha$ can be found analytically as a sum of the free modes of the system. The forced response $\chi = (u, v, h)$ is a sum of the free modes $\xi_m = (u_m, v_m, h_m)$, weighted by coefficients a_m

$$\chi = \sum a_m \xi_m, \quad (3.5)$$

where the coefficients are given by

$$a_m = \frac{1}{\alpha - i\omega_m} b_m, \quad (3.6)$$

where ω_m is the eigenvalue of the mode m , and

$$b_m = \left[\int \bar{\xi}_m(y) \sigma(y) dy \right] / \left[\int |\xi_m(y)|^2 dy \right]. \quad (3.7)$$

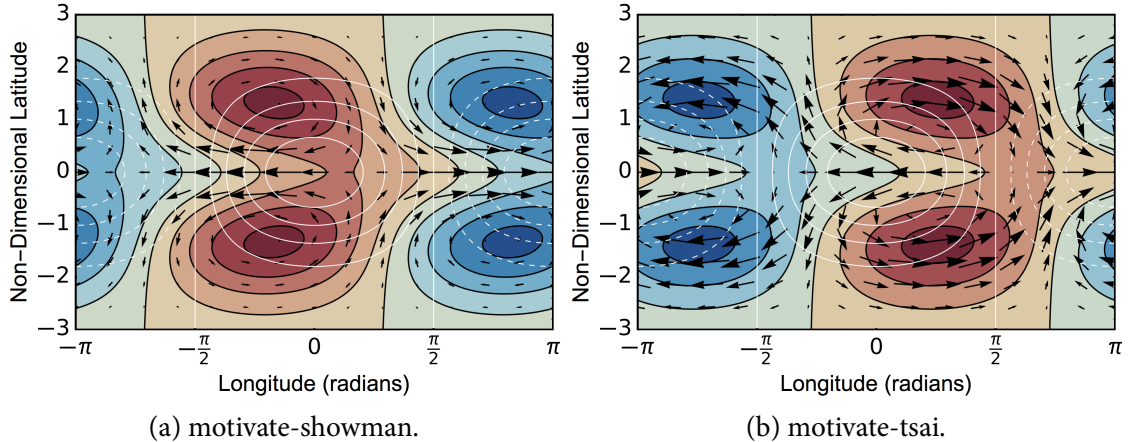


Figure 3.3: Forced solutions.

For the forcing $Q(x, y) = Q_0 \sin(x) e^{-y^2/2}$, all of the coefficients a_m are zero, apart from those for the Kelvin wave and the $n = 1$ Rossby wave. Figure 3.3a shows this forced response.

DO THIS! The eigenvalues determine the position of each free mode in the forced response.

In the rest of this chapter, I will instead use the pseudo-spectral method described in Appendix C to find the response to forcing. This method works for any forcing and background flow (unlike the analytic method), and still finds the exact analytic solution for this case with zero background flow. Figure 3.3a was actually calculated using this pseudo-spectral method rather than expanding in terms of the free modes, but the solution is identical (as explained in Appendix C, the basis functions of the pseudo-spectral method can exactly represent the free modes of the shallow-water system).

3.1.3 Wave Interactions with Flow

This flow can be approximated as uniform, and the resulting solutions for the free and forced modes are only slightly modified from the case with zero flow.

Figure 3.3b shows the response of Equation 3.1 to a forcing $Q(x, y) = Q_0 \sin(x) e^{-y^2/2}$, with a uniform background flow $\bar{U}(y) = U_0$. [Tsai et al. \(2014\)](#) shows that there is still an analytic solution for the forced response in a uniform background flow, with a uniform background height field. All of the modes comprising the forced response are Doppler-shifted eastwards by the background flow.

DO THIS PART BELOW!

The modes present in the forced response are shifted significantly by a zonal flow of non-dimensional magnitude XX. This depends on the eigenvalue.

In this chapter, I will build on these solutions by linearising these shallow-water equations around a non-uniform equatorial jet $\bar{U}(y)$ and its associated height perturbation $\bar{H}(y)$. This differs from [Showman and Polvani \(2011\)](#) which used zero background flow $\bar{U}(y) = 0$ and uniform background height $\bar{H}(y) = H_0$. It also differs from [Tsai et al. \(2014\)](#) which used uniform background flow $\bar{U}(y) = U_0$ and uniform background height $\bar{H}(y) = H_0$ (which is inconsistent – a geostrophically balanced uniform flow $\bar{U}(y) = U_0$ gives a non-uniform height field $\bar{H}(y)$).

3.2 Zonal Acceleration

This shallow-water system shows which stationary waves will be excited in the atmosphere of a tidally locked planet by the day-night forcing. The next step is to calculate the zonal acceleration produced by these stationary waves, and find the effect of the resulting flow on the waves themselves.

I will follow [Showman and Polvani \(2010\)](#) and [Showman and Polvani \(2011\)](#) to show that the classic Matsuno-Gill model introduced in the previous section predicts zero acceleration at the equator. An addition momentum transport term is required to represent the asymmetric momentum forcing due to vertical transport on the day- and night-sides [Shell and Held \(2004\)](#).

3.2.1 Acceleration in a Matsuno-Gill Model

Zonally averaging the zonal momentum equation in Equation 3.1 ([Thuburn and Lagneau, 1999](#)) ([Showman and Polvani, 2010](#)) gives the zonal acceleration profile in the shallow-water model:

$$\frac{\partial \bar{u}}{\partial t} = \underbrace{\bar{v}^* \left[f - \frac{\partial \bar{u}}{\partial y} \right]}_{I} - \underbrace{\frac{1}{\bar{h}} \frac{\partial}{\partial y} \left[(\bar{h}v)' u' \right]}_{II} + \underbrace{\frac{1}{\bar{h}} \bar{u}' Q'}_{III} - \underbrace{\frac{\bar{u}^*}{\tau_{\text{drag}}}}_{IV} - \underbrace{\frac{1}{\bar{h}} \frac{\partial (\bar{h}' u')}{\partial t}}_{(3.8)}$$

Figure 3.4 shows the different components of Equation 3.8 for the classic system of [Matsuno \(1966\)](#):

- Green line: Term I, zonal momentum transport by mean meridional circulation

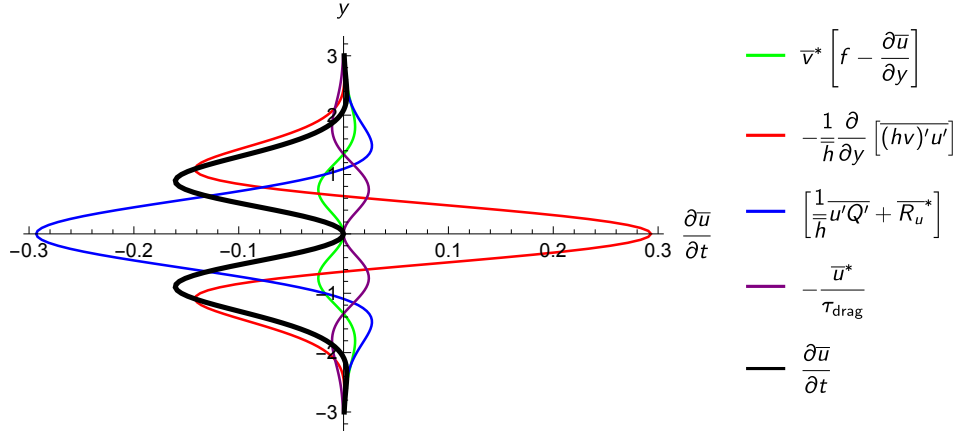


Figure 3.4: Acceleration terms.

- Red line: Term II, horizontal transport of zonal momentum
- Blue line: Term III, vertical transport of zonal eddy momentum
- Purple line: Term IV, zonal drag
- Black line: Left-hand-side, sum of all four terms.

Note that there is no contribution from the final term in Equation 3.8 as the solution is stationary.

The key point from Figure 3.4 is that there is zero zonal acceleration at the equator, so this model is not consistent with GCM simulations of tidally locked planets that show equatorial superrotation at the equator.

We can show that the acceleration must be zero at the equator for these forced shallow-water equations. Rewriting the zonal mean momentum equation in terms of the relative vorticity ζ (Thuburn and Lagneau, 1999) (Showman and Polvani, 2011)

$$\frac{\partial \bar{u}}{\partial t} = \bar{v}' \bar{\zeta}' + \bar{v}(f + \bar{\zeta}) - \frac{\bar{u}}{\tau_{\text{drag}}} + \bar{R}_u, \quad (3.9)$$

we see that as $v = 0$ at the equator (due to the symmetric forcing in y) $\frac{\partial \bar{u}}{\partial t} = 0$ at the equator also.

The fact that there is in the GCM simulations shows another process is affecting the zonal momentum at the equator. Note that this condition still applies to the same equations linearised about a zonal flow $\bar{U}(y)$ (Equation X).

3.2.2 Correction to Vertical Momentum Transport

The forced shallow-water equations predict zero zonal acceleration at the equator. So, there must be another process at work at the equator producing the eastward zonal flow seen in GCM simulations.

[Showman and Polvani \(2011\)](#) invoke a correction to the zonal momentum equation from [Shell and Held \(2004\)](#).

$$\begin{aligned} \frac{\partial u}{\partial t} - \beta y v + \frac{\partial h}{\partial x} &= R_u \\ \frac{\partial v}{\partial t} + \beta y u + \frac{\partial h}{\partial y} &= 0 \\ \frac{\partial h}{\partial t} + c^2 \left(\frac{\partial u}{\partial x} + \frac{\partial v}{\partial y} \right) &= Q(x, y) \end{aligned} \quad (3.10)$$

The correction R_u represents the effect of exchanging zonal momentum between the active layer and the lower layer. On the day-side, air with zero angular momentum rises from the substellar point into the active layer, giving a zonal acceleration which opposes the local u field. To conserve the vertically integrated local zonal momentum this acceleration

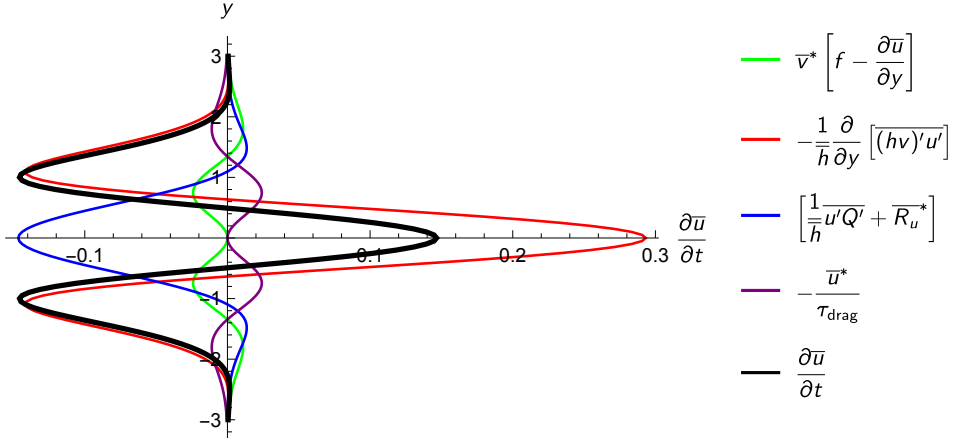


Figure 3.5: Acceleration terms with R.

is $R_u - \frac{Qu}{h}$ (Showman and Polvani, 2011). On the night-side, air leaves the active layer which does not affect the local angular momentum, so $R_u = 0$.

$$R_u = \begin{cases} -\frac{Qu}{h}, & Q > 0 \\ 0, & Q < 0 \end{cases} \quad (3.11)$$

This modifies the zonal mean momentum equation to:

$$\frac{\partial \bar{u}}{\partial t} = \underbrace{\bar{v}^* \left[f - \frac{\partial \bar{u}}{\partial y} \right]}_{I} - \underbrace{\frac{1}{h} \frac{\partial}{\partial y} \left[(\bar{h}\bar{v})' \bar{u}' \right]}_{II} + \underbrace{\left[\frac{1}{h} \bar{u}' \bar{Q}' + \bar{R}_u^* \right]}_{III} - \underbrace{\frac{\bar{u}^*}{\tau_{\text{drag}}} - \frac{1}{h} \frac{\partial (\bar{h}' \bar{u}')}{\partial t}}_{IV} \quad (3.12)$$

Figure 3.5 shows the terms Equation 3.12. In comparison to Figure 3.4, there is now a zonal acceleration at the equator.

Rewriting the zonal mean momentum equation in terms of the relative vorticity again shows that there is now a non-zero acceleration at the equator due to R_u :

$$\frac{\partial \bar{u}}{\partial t} = \bar{v}' \bar{\zeta}' + \bar{v}(f + \bar{\zeta}) - \frac{\bar{u}}{\tau_{\text{drag}}} + \bar{R}_u, \quad (3.13)$$

This explains the equatorial superrotation on tidally locked planets. But, it does not explain why momentum-conserving retrograde westward flow predicted by this shallow-water model in the mid-latitudes, does not appear in the GCM simulations, which instead have an atmosphere superrotating at most latitudes. In Chapter XX I will discuss this.

3.2.3 Equilibrium Equatorial Flow

This provides an estimate of the equilibrium zonal flow speed on the equator, which will occur when $\frac{\partial \bar{u}}{\partial t} = 0$:

$$\frac{\bar{u}}{\tau_{\text{drag}}} = \bar{R}_u, \quad (3.14)$$

As the zonal flow \bar{u} increases, the drag term $\frac{\bar{u}}{\tau_{\text{drag}}}$ will increase until it balances the acceleration due to vertical momentum transport \bar{R}_u .

The acceleration due to vertical momentum transport \bar{R}_u will also decrease as the zonal flow \bar{u} increases, so even if τ_{drag} is very large and $\frac{\bar{u}}{\tau_{\text{drag}}}$ is negligible, \bar{R}_u will eventually become zero for large enough zonal flow, and the acceleration will become zero. [Showman and Polvani \(2011\)](#) suggest that \bar{R}_u simply gets smaller as the zonal mean \bar{u} gets larger. Later, I will add the fact that the forced response is Doppler-shifted eastwards, changing the part of the eddy response that is on the day-side and contributes to \bar{R}_u .

In addition, I will show how this eastward shift decreases term II in Equation 3.12 by shifting the different wave components closer together. This further decreases the equato-

3.3. Wave Interactions with Shear Flow on the Beta-Plane

rial acceleration as the zonal flow increases, making it reach an equilibrium sooner.

3.2.4 Horizontal Momentum Transport from Stationary Waves

It is helpful to now consider the terms in Equation 3.8 in more detail.

Term II in Equation 3.8 is the horizontal momentum transport. The sign of Term II depends on the

But, it is cancelled out by the vertical momentum transport.

3.2.5 Horizontal Momentum Transport from Transient Waves

3.3 Wave Interactions with Shear Flow on the Beta-Plane

In this section, I discuss the main result of this chapter – the forced response of the shallow-water equations linearized around a zonally uniform shear flow $\bar{U}(y)$ and height $\bar{H}(y)$. I will show that the form of this forced response matches the results of GCM simulations, and suggest that the equatorial jet is therefore vital in controlling the global temperature structure and circulation pattern.

The background flow $\bar{U}(y)$ and height $\bar{H}(y)$ satisfy the second line of Equation 3.10, so are geostrophically balanced with $\bar{H}_y(y) = -y\bar{U}(y)$. For our Gaussian jet $\bar{U}(y) = U_0 e^{-y^2/2}$, the height perturbation is therefore $\bar{H}(y) = U_0 e^{-y^2/2}$ ([Hammond and Pierrehumbert, 2018](#)).

For the tests in this chapter, I use a forcing magnitude $Q_o = 1$ and equal radiative and dynamical damping rates $\alpha_{rad} = \alpha_{dyn} = 0.2$ ([Matsuno, 1966](#)). I will show the effect of

3.3. Wave Interactions with Shear Flow on the Beta-Plane

varying these damping rates in Section X.

The tests in this section will show the effect of a zonal flow with a maximum non-dimensional speed between 0 and 1, as this is the speed required for a significant zonal shift of the forced response, as discussed in Section X.

The value of $Q_0 = 1$ in the forcing $Q(y) = Q_0 \sin(x)e^{-y^2/2}$ was chosen to produce a comparable perturbation to that from the imposed equatorial jet, and to be consistent with [Matsuno \(1966\)](#) and [Showman and Polvani \(2011\)](#). Later in Section XX I will use a different (and more realistic) forcing value, to satisfy this condition in a spherical geometry with a different balance between jet velocity and jet height.

Linearised around the background flow $\bar{U}(y)$ and height $\bar{H}(y)$, the shallow-water equations in Section X become:

$$\begin{aligned} \frac{\partial u}{\partial t} + \alpha_{dyn}u + \frac{\partial \bar{U}(y)u}{\partial x} + \left(\frac{\partial \bar{U}(y)}{\partial y} - y \right)v + \frac{\partial h}{\partial x} &= 0 \\ \frac{\partial v}{\partial t} + \alpha_{dyn}v + \frac{\partial \bar{U}(y)v}{\partial x} + yu + \frac{\partial h}{\partial y} &= 0 \\ \frac{\partial \bar{H}'u}{\partial x} + \bar{H}'\frac{\partial v}{\partial y} - y\bar{U}(y)v + \frac{\partial h}{\partial t} + \alpha_{rad}h + \frac{\partial \bar{U}(y)h}{\partial x} &= Q(y) \\ \bar{H}' &= 1 + \bar{H}(y) \end{aligned} \tag{3.15}$$

To consider the free modes of this system, we set $Q(y) = 0$ and $\partial/\partial t = -i\omega$, and write u, v, h in the form $A(y)e^{i(k_x x - \omega t)}$:

3.3. Wave Interactions with Shear Flow on the Beta-Plane

$$\begin{pmatrix} \alpha_{dyn} + ik_x\bar{U}(y) & \frac{\partial\bar{U}(y)}{\partial y} - y & ik_x \\ y & \alpha_{dyn} + ik_x\bar{U}(y) & \frac{\partial}{\partial y} \\ ik_x\bar{H}' & -y\bar{U}(y) + \bar{H}'\frac{\partial}{\partial y} & \alpha_{rad} + k_x\bar{U}(y) \end{pmatrix} \begin{pmatrix} u \\ v \\ h \end{pmatrix} = i\omega \begin{pmatrix} u \\ v \\ h \end{pmatrix} \quad (3.16)$$

$$\bar{H}' = 1 + \bar{H}(y)$$

To find the stationary response to steady forcing, we set we set $Q(y) = Q_0 e^{-y^2/2}$ (Mat-suno, 1966) and $\partial/\partial t = 0$, giving the linear system of equations:

$$\begin{pmatrix} \alpha_{dyn} + ik_x\bar{U}(y) & \frac{\partial\bar{U}(y)}{\partial y} - y & ik_x \\ y & \alpha_{dyn} + ik_x\bar{U}(y) & \frac{\partial}{\partial y} \\ ik_x\bar{H}' & -y\bar{U}(y) + \bar{H}'\frac{\partial}{\partial y} & \alpha_{rad} + k_x\bar{U}(y) \end{pmatrix} \begin{pmatrix} u \\ v \\ h \end{pmatrix} = \begin{pmatrix} 0 \\ 0 \\ Q(y) \end{pmatrix} \quad (3.17)$$

$$\bar{H}' = 1 + \bar{H}(y)$$

I solved both the free and forced systems of equations using the method in Appendix X, expanding the solutions in terms of the parabolic cylinder functions. This method identifies the exact free and forced solutions in the case where $\bar{U}(y) = 0$, and finds the solutions with non-zero $\bar{U}(y)$ to better than 1 part in 10,000 when 30 basis modes are used in the calculation. In Appendix X, I show the accuracy of this method in more detail.

Finally, it is worth noting that I have considered the perturbations in the forced system to apply to a single shallow-water layer of height H_0 , non-dimensionalised to unity. Technically, the vertically varying heating profile in a planetary atmosphere excites a continuum of vertical modes, each defining a shallow-water system of different H_0 . However, Tsai et al. (2014) showed that in this forced shallow-water system, almost all of the energy is

3.3. Wave Interactions with Shear Flow on the Beta-Plane

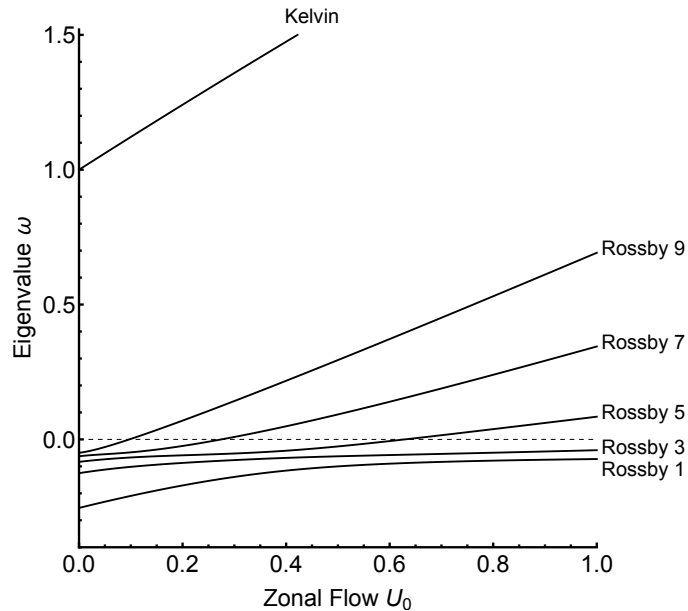


Figure 3.6: Eigenvalue shift.

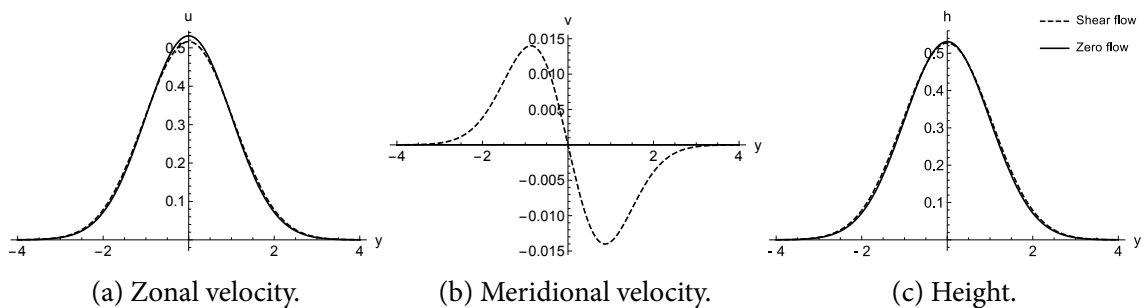


Figure 3.7: The meridional structure of the free Kelvin mode.

confined to the lowest-order vertical mode, making the assumption that a real atmosphere is described well by a single shallow-water layer reasonable.

3.3. Wave Interactions with Shear Flow on the Beta-Plane

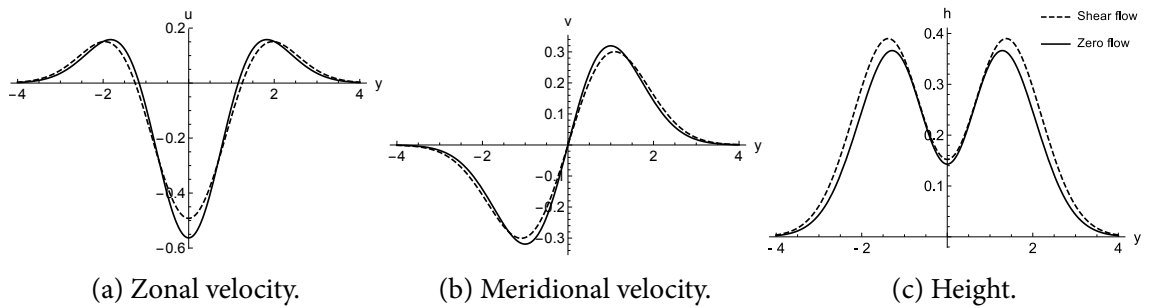


Figure 3.8: The meridional structure of the free Rossby mode ([Hammond and Pierrehumbert, 2018](#)).

3.3.1 Free Modes

In this section, I will discuss the effect of a background shear flow on the free modes of the shallow-water equations. This will be useful to understand the effect of the background flow on the forced response, in the next section.

In Section 3.1, I showed how the response to a forcing can be written as a sum of the free modes of the system. It is not possible to write down an exact solution like this when the system is linearised about a background flow $\bar{U}(y)$ and $\bar{H}(y)$, but it is still useful to interpret the resulting solution in terms of the fundamental free modes.

I will write the free solutions to shallow-water equations as a complex function of latitude $A(y)$, and the forced solutions as functions of both latitude and longitude in the form $A(y)e^{i\delta(y)x}$. This phase $\delta(y)$ determines the longitudinal structure of the forced response, and is equivalent to the phase shift $(\omega_m - k_x \bar{U})$ derived for a uniform flow in Section XX.

We can still consider the response to forcing as a sum of the free modes of the system, as in Section X. Now the equations are linearised about a shear flow $\bar{U}(y)$ and $\bar{H}(y)$, the free modes have a different latitudinal structure $u(y), v(y), h(y)$ and have different

3.3. Wave Interactions with Shear Flow on the Beta-Plane

eigenvalues ω_m (so will have different longitudinal position in the forced response).

I found the free modes of the shallow-water system defined by Equation 3.16 using the method in Appendix X. Figure 3.6 shows the real parts of the eigenvalues of the free Kelvin mode and the symmetric free Rossby modes of Equation 3.16, for a background flow $\bar{U}(y) = U_0 e^{-y^2/2}$ with a variable magnitude U_0 ([Hammond and Pierrehumbert, 2018](#)). I plot these modes as they are the lowest-order (so largest magnitude) modes excited by the symmetric, stationary forcing.

The value and sign of these eigenvalues determine the position of the free mode in the forced response, similar to Equation X in Section X. Note that an exact forced solution in terms of a series free modes is now not possible as the flow is not uniform, but it is still very useful to interpret the forced response in this way.

As the magnitude U_0 of the equatorial jet $\bar{U}(y)$ increases, all of the eigenvalues of the free modes become more positive, corresponding to an eastward shift in their position in the forced response (as in Equation X in Section X). The Kelvin mode already has a positive eigenvalue for $U_0 = 0$ (hence its position in Figure 3.3a), and this becomes larger as U_0 increases, so the Kelvin mode becomes further east in the forced response. The maximum shift of the modes is to +90° east of the substellar point (as in Equation X), no matter how large the eigenvalue becomes. This shift leads to the large eastward equatorial hot-spot shift that will be seen later.

The Rossby modes are a little more complicated. [Tsai et al. \(2014\)](#) shows that in a uniform background flow, the $n = 1$ Rossby mode is shifted eastwards towards +90°, producing a hot-spot shift (reproduced in Figure 3.3b). In fact, Figure 3.6 shows that in this non-uniform flow $\bar{U}(y)$, the $n = 1$ Rossby mode eigenvalue becomes less negative but does not

3.3. Wave Interactions with Shear Flow on the Beta-Plane

become positive for $U_0 = 1.0$. This means that in the forced response it is shifted eastwards, but not far enough to pass the substellar point.

The higher order Rossby modes are shifted by the flow $\bar{U}(y)$, as shown by their positive eigenvalues for high enough flow speed U_0 . However, the higher the order of a mode, the weaker its contribution to the forced response ([Matsuno, 1966](#)). The $n = 3$ and $n = 5$ symmetric Rossby modes are still important to the forced response, but any modes beyond this are less important.

That is not to say that the $n = 1$ mode is never responsible for the hot-spot shift – later, we will show that in a spherical geometry the $n = 1$ mode shifts close to $+90^\circ$ eastwards. It is also possible in the beta-plane system for different input parameters (flow speed, damping rates) to shift the $n = 1$ Rossby mode past the substellar point. But, our free mode expansion has shown that the $n = 1$ Rossby mode is not the only important mode, and that the higher-order modes are also important to the forced response.

For zero damping, half of these eigenvalues will have positive imaginary parts, and the modes corresponding to them will grow exponentially. Non-zero damping decreases the imaginary part of all the modes, so will make some or all of these modes stable. In general, the free linear system in Equation 3.16 will have some unstable modes unless the damping is very large. These unstable modes are similar to those discussed by ?, who show how similar modes can produce superrotation even on a planet without a permanent day-night heating difference.

These unstable modes technically make the linear forced wave problem ill-posed, since the result of any linear initial value problem will be eventually dominated by the most

3.3. Wave Interactions with Shear Flow on the Beta-Plane

rapidly growing modes rather than the stationary response. Later comparison with nonlinear GCM simulations in Section ?? will show that the forced response still has considerable explanatory power. This may be because in reality the unstable modes equilibrate due to damping or nonlinear effects, at a sufficiently low amplitude that they take the form of mobile waves propagating across the forced stationary pattern without significantly disrupting its basic structure. Future work should investigate the exact nature of these instabilities, and the effect of damping and shear flow on their growth rates.

The shear flow also affects the latitudinal structure $A(y)$ of the modes. The lowest-order free solutions of Equation 3.16 (the Kelvin and Rossby modes), plotted in Figure 3.8 and 3.7, resemble the free solutions with zero shear flow ([Matsuno, 1966](#)), with their latitudinal structure slightly changed by a **weak shear flow** $\bar{U} = 0.1e^{-y^2/2}$. The shear flow perturbs the solutions by adding higher order meridional structure. For example, the meridional wind of the Rossby wave in Figure 3.8 resembles the **$n = 1$ parabolic cylinder function** added to the $n = 3$ function (see Figure C.1a in Appendix ??). [Boyd \(1978\)](#) discusses how a shear flow affects the meridional structure of these modes in more detail.

3.3.2 Forced Solutions

Figure X shows the forced solution in shear flow.

3.3.3 Equilibrium Circulation

The equatorial superrotation reaches a steady equilibrium when the zonal acceleration is zero.

3.3. Wave Interactions with Shear Flow on the Beta-Plane

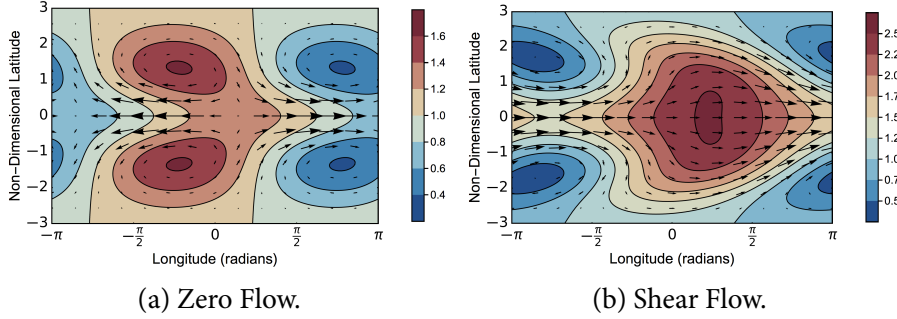


Figure 3.9: Zero Flow and Shear Flow.

As discussed in Section 3.2, the equatorial acceleration decreases as the zonal flow increases, reaching an equilibrium when the acceleration is zero.

3.3.4 Damping

Figure X shows the effect of different damping rates.

3.3.5 Hot-Spot Shift

What is the relevance of these forced solutions for the atmospheres of tidally locked planets, and interpreting observations of them?

It is possible to match up the shifted eigenvalues of the free modes in Section X to the total forced response in Section X to understand the change in global temperature structure produced by the equatorial jet.

3.4 Wave Interactions with Shear Flow on a Sphere

The beta-plane solutions are intuitive but less accurate for a sphere.

3.4.1 Spherical Shallow-Water Equations

3.4.2 Forced Solutions

3.5 Scaling Relations

3.5.1 1D Scaling Relations

3.5.2 2D Scaling Relations

3.6 Other Jet Patterns

The suite of tests in Chapter XX show that the zonal mean wind profile on a tidally locked planet is not always well represented by a Gaussian. There can be only two jets in the midlatitudes, or three jets, one on the equator.

In this section I find the forced response with different jet profiles, and show that the result is not particularly different to the Gaussian jet used up to this point.

CHAPTER 4

Non-Linear Tests of a Linear Theory of Tidally Locked Atmospheres

“One might as well approximate the derivatives well instead of badly”

— John P. Boyd, *Chebyshev and Fourier Spectral Methods*

In this chapter, I test the mechanism for the circulation of tidally locked planetary atmospheres predicted in the previous chapter. I use a single-layer non-linear shallow-water model, and a 3D General Circulation Model (GCM) to simulate the atmosphere, and compare the results to the linear theory.

The linear theory simplified the system of a tidally locked planetary atmosphere greatly, and these tests will investigate whether these assumptions were accurate, and test how well the theory predicts the equilibrium circulation.

I will introduce the models used, and show basic tests of whether the mechanism predicted by the linear model is actually at work. I will test the spin-up and equilibrium states of the non-linear models, and compare the results to the scaling relations predicted by the linear model.

4.1. Non-Linear Tests of Linear Shallow-Water Theory

This chapter will show that the linear model is a good approximation to the results of the non-linear simulations. The wave-mean flow interaction in the linear theory also applies to the non-linear simulations, suggesting that this is at work on real tidally locked planetary atmospheres as well.

4.1 Non-Linear Tests of Linear Shallow-Water Theory

The linear model in Chapter 3 made X main simplifications:

1. The perturbations to the atmosphere are small enough to be approximately linear.
2. The atmospheric response is (on average) stationary, and any transient behaviour does not affect the mean circulation.
3. The atmosphere and the variations in it are small enough in the vertical to be approximated by a shallow model.
4. The day-night forcing is approximated by a relaxation to a constant radiative equilibrium height field.

This section discusses tests of the single-layer linear theory in Chapter 3 using a single-layer non-linear model, which removes the first two assumptions.

Non-Linear Shallow-Water Model

I used the Geophysical Fluid Dynamics Laboratory Flexible Modelling System (FMS) Spectral Dynamical Core (GFDL-SDC) for non-linear shallow-water simulations. Appendix B describes the model setup.

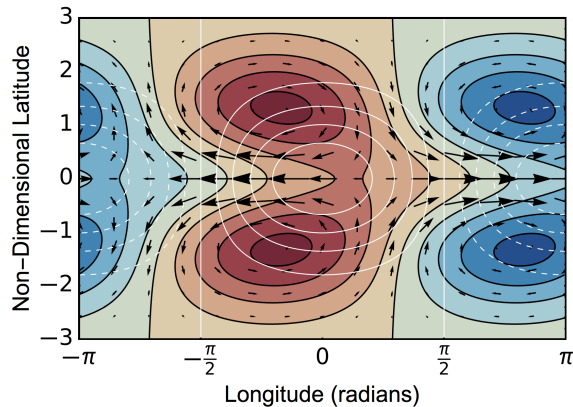


Figure 4.1: The linear response.

Testing Linearity

The linear model in Chapter 3 is based on a forced linear shallow-water system as discussed in [Matsuno \(1966\)](#). Figure 4.1 shows the response to a forcing $Q(x, y) = \sin(x)e^{-y^2/2}$ in this linear system.

The linear model assumes that the perturbations in the shallow-water system (representing perturbations in a real three-dimensional atmosphere) are small enough that the linear terms dominate the shallow-water equations. I ran simulations in the non-linear shallow-water model to test whether they matched the linear model at appropriate forcing strength.

The non-linear shallow-water equations are:

The linear solution in spherical coordinates in Figure X in Chapter X has $\alpha_{rad} = \alpha_{dyn} = 0.2$, $G = 1$ and $\Delta h/H = 0.5$. To match this in the non-linear model, I set $\alpha_{rad} = \alpha_{dyn} = 0.2$, $\Delta h = 5$ km, and $H = 10$ km. To set $G = 1$, I set $R = R_{Earth}$ and $g = 10$, then tuned the rotation rate to $\Omega = 4.964 \times 10^{-5} = 0.6807\Omega_{Earth}$.

4.1. Non-Linear Tests of Linear Shallow-Water Theory

Figure 4.2 shows the equilibrated height and velocity fields for the non-linear model with these parameters, and zero imposed background flow. The non-linear model matches the linear model in Figure X well, with a similar pattern and perturbation size. There is a small day-night asymmetry in the non-linear mode which is not present in the linear model.

The plots in Figure 4.3 show the non-linear response with a smaller height perturbation $\Delta h = 1$ km, and a larger height perturbation $\Delta h = 20$ km. Figure 4.3a with the smaller perturbation has a smaller day-night asymmetry than Figure X.b, which is expected as the smaller perturbation should produce a more linear response. Figure 4.3b with the larger perturbation has a larger day-night asymmetry than Figure 4.2, which is expected as the larger perturbation should produce a less linear response. The pattern is also more different from the linear pattern, showing that the linear approximation is less appropriate at the higher forcing amplitude.

This is all as expected, and shows that the forcing amplitudes used in the linear solutions in Chapter X ($\Delta h/(H\tau_{rad} \sim 0.1)$) and the GCM simulations in Chapter X ($\Delta T/(T \sim 0.1)$) are in a regime that is well represented by the linear approximation.

It is possible that the background flow that is imposed in the linear solutions and emerges in the GCM simulations affects the size of the perturbations and moves the system out of the linear regime. I ran the same non-linear shallow-water simulations as Figure X, but imposed the same jet as in the linear solutions to test if the linear and non-linear solutions still matched.

The simulations had the same parameters as in Figure 4.2. The linear model in spherical geometry in Chapter X has a jet with a non-dimensional velocity of

4.1. Non-Linear Tests of Linear Shallow-Water Theory

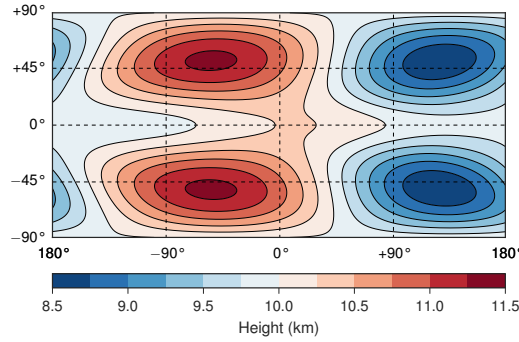


Figure 4.2: 5e3.

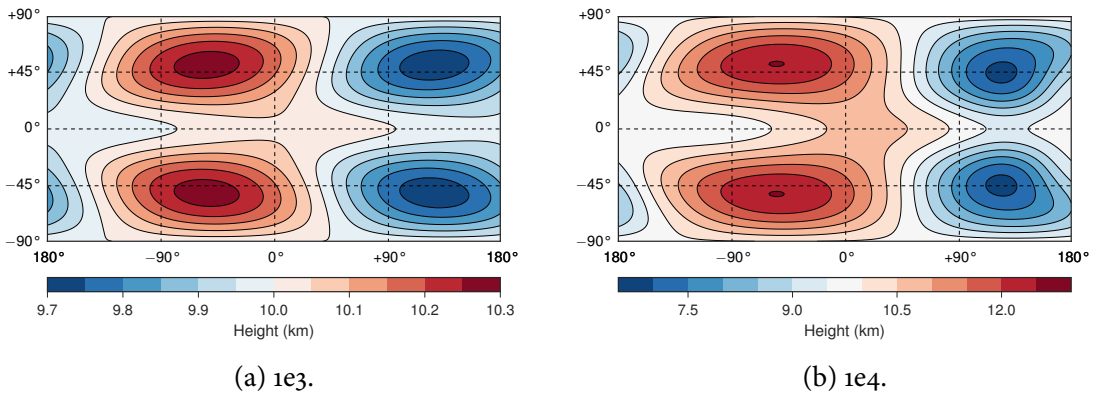


Figure 4.3: Nonlinear.

$0.5 \cos \phi \exp(-(\phi/\phi_0)^2)$, with a jet width $\phi_0 = \pi/3$. The non-linear system in Figure 4.2 has a velocity scale of $R\Omega$, so I relaxed the non-linear simulations on a timescale $\tau_{dyn} = 1/\alpha_{dyn}$ to a background flow profile $R\Omega \cos \phi \exp(-(\phi/\phi_0)^2)$. Figure 4.4 shows the equilibrated response.

The non-linear response has much less shift at higher latitudes, and a much narrower zonal height field. The zonal flow profile is much narrower than the imposed profile. Figure X shows that subtracting the background flow that is imposed leaves a large retrograde

4.1. Non-Linear Tests of Linear Shallow-Water Theory

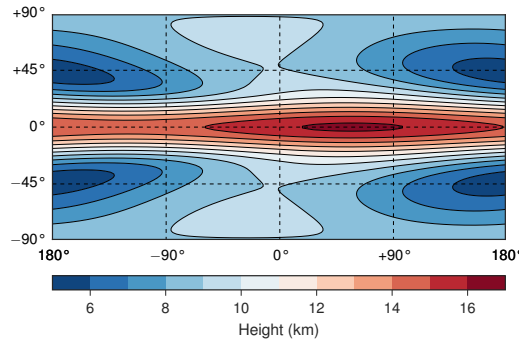


Figure 4.4: Matsuno jet control.

flow in the midlatitudes, as forms in the non-linear Matsuno case. Figure X shows the response and the mean zonal velocity of the case which is not relaxed towards a background flow (the same test as Figure 4.2). This case has westward flow in the midlatitudes, as predicted by Figure X in Chapter X. This mechanism causes the reduced eastward flow in the midlatitudes in the case with a jet in Figure X.

This is responsible for the main difference between the linear and non-linear model. In fact, the acceleration calculated in the linear model does predict this westward midlatitude flow, but it was ignored in Chapter X to match the GCM results.

This highlights a difference between the GCM and the shallow-water models. The shallow-water models always predict a westward acceleration in the mid-latitudes, but this is rarely seen in the GCM. In Chapter X I suggest that eastward acceleration from Rossby wave breaking is responsible for the midlatitude eastward flow in the GCM.

These simulations have shown that the linear model is an appropriate approximation for the atmosphere of a tidally locked planet, but that it does not correctly predict the acceleration away from the equator.

4.1. Non-Linear Tests of Linear Shallow-Water Theory

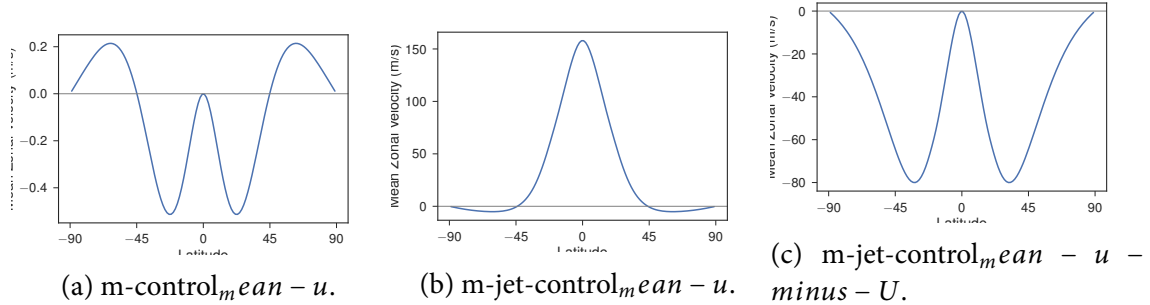


Figure 4.5: Nonlinear with and without imposed jet.

Testing R Term

[Showman and Polvani \(2010\)](#) shows that the R term in Chapter X is vital to the equatorial superrotation seen on tidally locked planets.

Figure X shows the height field and mean zonal wind of the non-linear shallow-water model with this R term added. Similar to Figure X in [Showman and Polvani \(2010\)](#), it shows equatorial superrotation.

It has the same parameters as Figure X but has the R term added, which is why it has equatorial superrotation but Figure X does not. Section X in Chapter X shows how the R term produces this effect, as does Figure X in Chapter X.

Like Figure X in [Showman and Polvani \(2010\)](#), there is a retrograde flow in the midlatitudes (where the prograde momentum is transported out of). This retrograde flow is not seen in the GCM, so there must be another effect involving vertical transport of retrograde momentum out of this layer.

Figure X shows tests with different parameters, showing how the equatorial jet speed depends on the parameters. For the default parameters of XX, the equatorial jet is very

4.1. Non-Linear Tests of Linear Shallow-Water Theory

slow. For the parameters X, the jet speed is comparable to the GCM results in Section X.

Testing Zonal Flow Profile

The zonal flow profile in Figure 4.5a matches the predicted shallow-water acceleration with R in Chapter X.

ALSO DO TEST WITHOUT R!

Testing Equilibrium State

Chapter X discusses the jet acceleration.

The time-stepped model reaches an equilibrium state after about X days. The transient response from the impulse generated by turning on the forcing dissipates, and a steady state is reached.

Show wave components, hot-spot, and wind directions.

Figure X shows the equilibrium state for the model with forcing X and rotation rate X.
Figure X shows the eddy state, showing how the waves have shifted.

Testing Jet Spin-up

I ran tests to show how the atmosphere reaches this state.

Figure X shows the eddy state over time of the previous test.

Figure X shows the Rossby and Kelvin components over time of the previous test.

Spin-up of height field, eddy height field, and Rossby and Kelvin components.

Scaling Relation Tests

Test effect of rotation rate, forcing, jet speed.

Figure X shows the equilibrium state for the model with the same forcing X and different rotation rates X.

Figure X shows the equilibrium state for the model with different forcing X.

Figure X shows the equilibrium state for the model with different jet speed X.

4.2 GCM Tests of Shallow-Water Theory

I used the GCM Exo-FMS, based on the Geophysical Fluid Dynamics Laboratory Flexible Modelling System (GFDL-FMS). Chapter ?? and Appendix A describe this model.

Testing Equilibrium State

Show wave components, hot-spot, and wind directions.

Testing Jet Spin-up

Spin-up of height field, eddy height field, and Rossby and Kelvin components.

Scaling Relation Tests

Test effect of rotation rate, forcing, jet speed.

CHAPTER 5

Equilibrium Circulation States on Tidally Locked Planets

“Very strange,” he said. “A permanent anticyclone, and inside a huge, calm land that never sees a storm and never has a drop of rain.”

“Good place for a holiday then!”

— Terry Pratchett, *The Last Continent*

Tidally locked planetary atmospheres

5.1 Equilibrium Flow Profile

Chapter X showed that the global circulation and temperature distribution of an atmosphere on a tidally locked planet depends greatly on the zonal jets present on the planet.

Equatorial Acceleration

Midlatitude Acceleration

Surface Drag

Equatorial Flow Direction

Number of Jets

GCM Simulations

Figure X shows a suite of tests (P+H2019) showing how the number of jets varies with rotation rate and temperature.

Figure X shows the spin-up of a very rapidly rotating case.

5.2 Initial Conditions

Starting from Rest

Initially Retrograde Flow

Initially Strong Prograde Flow

5.3 Instabilities as deviations from equilibrium

Linear Model Instability Analysis

The linear model predicts instabilities.

Instabilities in GCM

Instabilities appear in the GCM

5.4 Jet Scaling Relations

Equatorial versus Midlatitude Jets

CHAPTER 6

Linking the Climate and Thermal Phase Curve of 55 Cancri e

*“One face is forever sunlit, and one forever dark, and only the planet’s slow lib-
eration gives the twilight zone a semblance of seasons.”*

— Stanley G. Weinbaum, *The Lotus Eaters*

Now that I have introduced lava planets and 55 Cancri e in Chapter 2, laid out a theory of their circulation in Chapters 3 and X, and discussed the numerical model I used to simulate them in Chapter ??, I can move to the central question of this thesis. Namely, how to interpret the thermal emission phase curve of a tidally locked lava planet? The remaining chapters of my thesis will investigate this in increasing detail.

The first phase curve of a Super-Earth was measured by [Demory et al. \(2016\)](#) using Spitzer observations of 55 Cancri e, following the measurement of transits in the visible ([Winn et al., 2011](#)) and infrared ([Demory et al., 2011](#)). This presented the first observation directly linked to the global circulation of a terrestrial planet outside our solar system. It provides an opportunity to test the theories and simulations of the atmospheric circulation

of a tidally locked planet that have been shown previously in this thesis.

The thermal phase curve of 55 Cnc e presents the possibility of testing this picture of lava planets, and in particular to determine whether the phase curve demands the presence of a thick noncondensable background atmosphere. In this paper, we use a general circulation model (GCM) to model a range of hypothetical climates for 55 Cnc e and reconstruct their thermal phase curve, in order to test whether the observed phase curve is inconsistent with the presence of a thick atmosphere. We explore which atmospheric compositions are compatible with the phase curve. The results we have obtained for 55 Cnc e will carry over readily to the interpretation of other lava planet phase curves when they become available. The general utility of thermal phase curves in determining characteristics of exoplanets and their atmospheres has been discussed in Selsis et al. (2011) and Maurin et al. (2012).

The analysis in this paper builds on the results of Cowan Agol (2011), Menou (2012), and Komacek Showman (2016), who explored the effect of parameters such as the mean molecular weight on the thermal phase curve of Hot Jupiters via the radiative and advective timescales. Koll Abbot (2015) modelled the relation between atmospheric properties and broadband thermal phase curve for terrestrial planets in a regime (expected to be appropriate to most tidally locked planets) with a significant phase curve amplitude, but very little hot-spot offset. We have identified a regime which can support both a notable amplitude and offset.

Section 2 describes our model and explains the physical processes which it includes. Section 3 lays out the current theory of global circulation on tidally locked planets, where we discuss the key nondimensional parameters and situate 55 Cnc e in the space of circulation regimes. We describe the results from our experiments in Section 4, focusing on

their temperature distributions and simulated phase curves in comparison to the results of Demory et al. (2016b). Further interpretation of the results is provided in Section 5 and our principal findings are summarized in Section 6.

Our best-fit clear-sky atmosphere has a surface pressure of 5 bar and a mean molecular weight of 4.6 gmol¹. This molecular weight would support the hypothesis of an H₂-rich atmosphere; however, it is the observed hot-spot phase shift which favours low molecular weight, underscoring the importance of accurate measurements of this quantity for future observations of 55 Cnc e and other lava planets. A diagnostic estimate of cloud effects indicates that Na clouds would not form in such an atmosphere, but that SiO clouds could form on the night-side and bring the modeled night-side brightness temperature more in line with observations. Our results on the vertical structure of the temperature pattern underscore the importance of future measurements of spectrally resolved phase curves for 55 Cnc e and other lava planets, which would provide an important window into atmospheric composition and dynamics.

In the next chapter, I will show how we coupled a more realistic radiative transfer scheme and a dynamic cloud model to Exo-FMS, in order to test the questions raised by this chapter.

6.1 Observations of 55 Cancri e

55 Cancri e

The first phase curve of a Super-Earth was measured by Demory et al. (2016b) using Spitzer observations of 55 Cancri e, following the measurement of transits in the visible

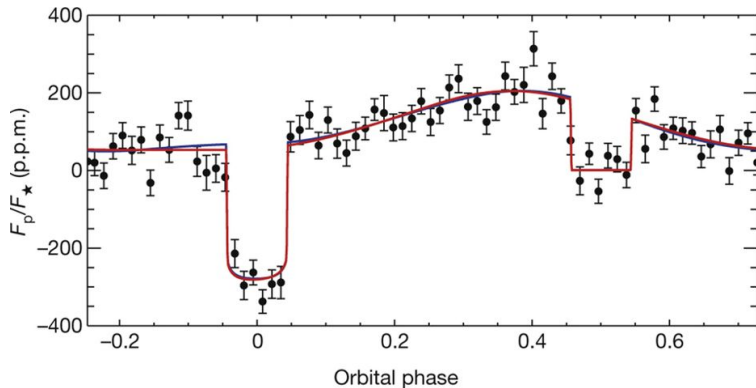


Figure 6.1: Phase curve.

(Winn et al. 2011) and infrared (Demory et al. 2011). 55 Cnc e is a Super-Earth discovered by McArthur et al. (2004) with mass $8.63 M_{\oplus}$ and radius $2.00 R_{\oplus}$ in a close, tidally locked orbit with period 0.737 days.

Thermal Phase Curve

The thermal phase curve has a large amplitude and an offset between its secondary eclipse and its phase maximum. Demory et al. (2016b) used the curve to reconstruct a temperature map with a maximum hemisphere-averaged $4.5\mu\text{m}$ brightness temperature of (2700 ± 270) K, day-night contrast of (1300 ± 670) K, and a hot-spot shifted eastwards by (41 ± 12) ■

Possible Atmosphere

55 Cnc e is a member of a class of planets known as “lava planets” which are in such close orbits that they are likely to be tide-locked and have a permanent dayside magma ocean. It

6.1. Observations of 55 Cancri e

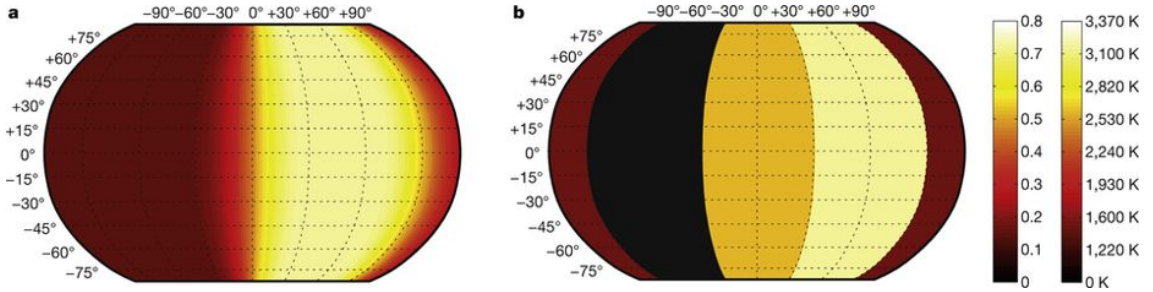


Figure 6.2: Temperature map.

has been argued that the atmospheres of such planets could consist of thin mineralvapour atmospheres outgassed from the magma ocean (L'eger et al. 2011) (Castan Menou 2011). Such thin atmospheres, consisting of a few millibar or less surface pressure, cannot transport much heat apart from possible lateral heat redistribution within the magma ocean, so would yield a phase curve very similar to that of an airless rocky planet with a very cold night-side such as discussed by Maurin et al. (2012).

The transit depth spectra reported in Tsiaras et al. (2016) require a thick H₂-rich atmosphere. However, Lammer et al. (2013) calculated that an H₂ atmosphere on 55 Cnc e would have a hydrodynamic escape rate of up to 2.8×10^9 gs⁻¹. This implies that a 10 bar atmosphere would be lost in less than one million years, making it implausible that an H₂-rich atmosphere could be maintained on this planet. However, the study of exoplanets has yielded up many objects that according to previous conceptions should not exist, so in this paper we will take the idea of an H₂-rich atmosphere seriously, and ask what features of the phase curve measured by Demory et al. (2016b) are compatible with, or demand, a low molecular weight atmosphere. In order to focus on dynamical behavior in this initial study, we make a number of simplifying assumptions regarding the radiative be-

havior of the atmosphere. First, we assume the atmosphere to be transparent to incoming stellar radiation, so that all of the shortwave radiation is absorbed at the ground, leading to a deep day-side convective layer. This assumption is based on estimates of the shortwave opacity of likely cloud-free atmospheres of up to 10 bars. The addition of a small amount of shortwave opacity would not change our results much, so long as atmospheric absorption occurs near enough the surface to drive a convective troposphere. Very thick shortwave-opaque atmospheres could instead have a deep radiative-equilibrium layer with a thin dynamically active layer near the top; we shall not consider such atmospheres in the present paper. In the infrared, the atmosphere is assumed to act as a grey gas with specified optical thickness and opacity. This is not inconsistent with the assumption of an atmosphere largely transparent to incoming stellar radiation, because 55 Cancri is a G star, with a relatively low proportion of its output in the near-IR. The use of gray gas radiation for climate calculations is not a serious source of inaccuracy as the circulation is primarily affected by the radiation scheme via the surface temperature relative to the radiating temperature of the planet. The optical thickness can be tuned to match the temperature that would be yielded by an assumed real-gas atmosphere, so in this paper we use primarily as a way to control surface temperature. Non-grey radiative effects are taken into account when we interpret the results in terms of the corresponding Spitzer $4.5\mu\text{m}$ phase curve, in that we consider the emission from a range of different atmospheric levels and not just the grey radiating level. This allows for the possibility that the atmospheric composition may support an infrared window region near $4.5\mu\text{m}$, allowing radiation from deeper in the atmosphere, or a source of anomalous opacity (e.g. clouds) there, forcing the radiating level to be higher in the atmosphere. The surface pressure determines the atmospheric mass

via the hydrostatic relation. For a given surface pressure and , atmospheric composition affects the climate through mean molecular weight and specific heat. However, molar specific heat is only weakly dependent Climate of 55 Cancri e 3 on composition, because it is primarily determined by the number of active degrees of freedom. For example, at 2000K the molar specific heats of CO, N₂ and H₂ vary by no more than 3.435.5 Jmol⁻¹K⁻¹ , with similar results for other common diatomic gases. Triatomic gases have only a modestly greater molar specific heat at 2000K, e.g. 60 for CO₂ or 46 atmosphere's ability to transport heat, is mostly determined by surface pressure and molecular weight. The mean molecular weight also affects the speed of gravity waves in the atmosphere, through its influence on the gas constant. This speed determines the character of many atmospheric waves which directly transport heat and are implicated in the generation of super-rotating low-latitude jets, which also transport heat. We present our simulation results in terms of a range of H₂-N₂ mixtures, but they would apply accurately to any other diatomic mixture with the same molecular weight, and with only moderate inaccuracy to triatomic-dominated mixtures.

Atmospheric Circulation

The measured phase curve of 55 Cnc e exhibits two features that demand substantial horizontal heat transport. First, the hot spot of the planet is shifted 41° eastward relative to the substellar point. Second, the nightside temperature of the planet is quite high – on the order of 1300K – demanding delivery of $1.6 \times 10^5 \text{ W/m}^2$ of heating to maintain it. However, the day-night temperature difference is also large – on the order of 1300K – which puts a limit on the efficiency of the heat transporting mechanism. It has been sug-

gested that the implied heat transport on 55 Cnc e might be carried by the magma ocean. However, Kite et al. (2016) argued that a magma ocean could not redistribute enough heat to affect a planet’s measured phase curve. It is also conceivable that tidal heating could contribute to maintaining the night-side temperature. In this paper, we will focus on the question of whether atmospheric heat transport alone can account for the phase curve, though we will offer some remarks in Section 5 on problems with tidal heating as an explanation of the night-side temperature. The hot-spot phase shift and phase curve amplitude on tide-locked planets have been extensively studied in connection with interpretation of Hot Jupiter phase curves. For sufficiently short period orbits, the global circulation of such atmospheres is dominated by the effects of planetary scale equatorial Rossby and Kelvin waves which drive a superrotating jet (Showman Polvani (2011), Heng Showman (2015)). The circulation system transports heat eastwards around the equator, shifting the hot-spot from the substellar point and warming the night-side of the planet. The observed phase curve of 55 Cnc e poses the particular challenge that its large 41 \pm hot-spot shift suggests strong heat redistribution, but its large 1300 K day-night difference suggests weak heat redistribution. The need to negotiate the tension between these two requirements puts strong constraints on the kind of atmosphere the planet can have.

6.2 Simulating a Lava Planet

6.3 Simplified Scaling Theory

6.4 Idealised Simulations

6.4.1 Mean Molecular Weight

6.4.2 Surface Pressure

6.4.3 Optical Thickness

6.4.4 Vertical Structure

6.4.5 Phase Curves

6.5 Discussion

CHAPTER 7

Clouds on Lava Planets

“One face is forever sunlit, and one forever dark, and only the planet’s slow liberation gives the twilight zone a semblance of seasons.”

— Stanley G. Weinbaum, *The Lotus Eaters*

Cloud-covered exoplanets are a great problem for exoplanet observers, turning illuminating spectra into flat lines. Uniform cloud cover can be an issue, but heterogenous cloud cover may be useful.

Hot Jupiters are suggested to have cloud cover. Lava planets could have

In this chapter, I address the outstanding question from Chapter X – could the difference between our model results of 55 Cancri e and the observed low night-side temperature be due to high night-side clouds? I also discuss the effect of clouds on global circulation

and on observables such as hot-spot shift.

7.1 Clouds on Lava Planets

7.2 Simulations of Clouds

7.3 Effect on Observations

CHAPTER 8

Introduction

“Any finite number divided by infinity is as near to nothing as makes no odds, so the average population of all the planets in the Universe can be said to be zero. From this it follows that the population of the whole Universe is also zero, and that any people you may meet from time to time are merely the products of a deranged imagination.”

— Douglas Adams, *The Restaurant at the End of the Universe*

Lava planets are rocky, very hot, and orbit so close to their host stars that they are expected to be tidally locked to them. This means that they always present the same side to the star, so have a permanent day-side and night-side. This thesis investigates the question of what these properties mean for the atmosphere of the planet, particularly its circulation and composition. Tidally locked planets are very common and observable. Lava planets are particularly observable, especially for rocky planets.

Why are tidally locked planets important? Their unusual situation could make them seem like oddities, unrelated to the majority of planets. On the contrary, Figure 8.1 shows that a large fraction of known exoplanets are expected to be tidally locked. It shows the stellar masses and semi-major axes for all exoplanets listed on the NASA Exoplanet Archive

at the time of writing, with all the planets below the line expected to be tidally locked ([Pierrehumbert and Hammond, 2018](#)).

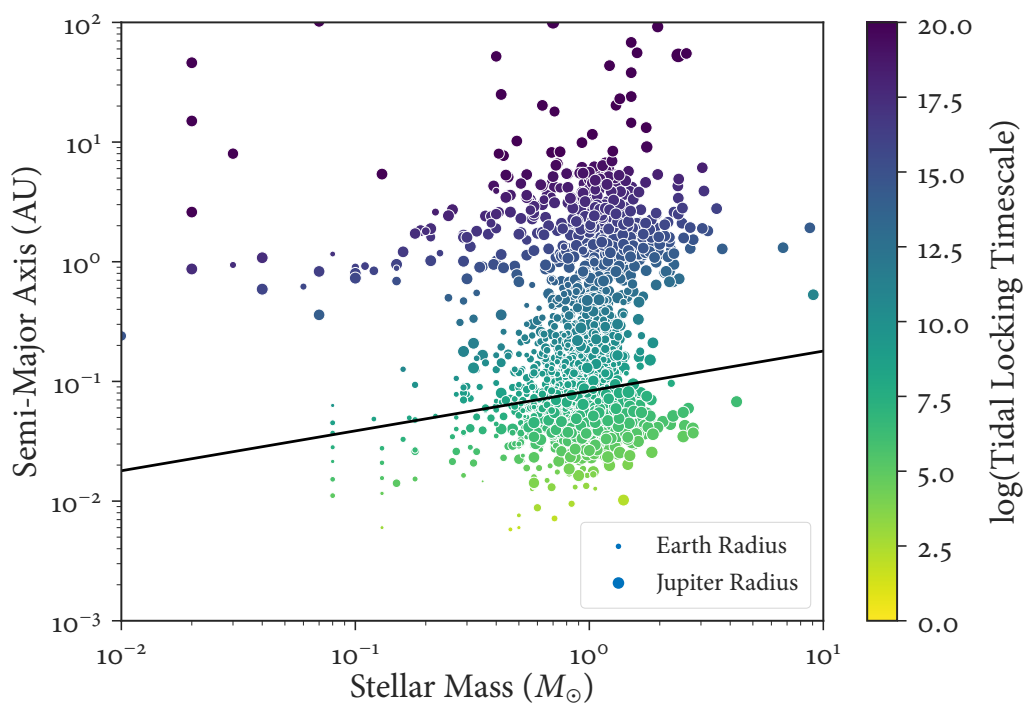


Figure 8.1: The population of known exoplanets plotted by semi-major axis and stellar mass. All the planets below the line have a timescale to reach a tidally locked state of less than 0.1 billion years, so are expected to be in this state.

These planets are also generally more easily characterised than the others, giving larger signals for spectroscopy when they transit their stars. This tendency may have created a detection bias, where close-in exoplanets are more likely to be detected so it appears that a greater fraction are tidally locked than is actually the case. Even if this is true, it does not detract from the relevance of tidally locked planets – we can only study planets we know about!

In Chapter 1, I discuss the concept of a “lava planet” and review the literature of discovery, characterisation, and modelling of such planets. I aim to introduce the scientific concepts and questions that I will address through the rest of the thesis.

In Chapter 2, I discuss the theoretical work I did to understand the global circulation of tidally locked planets in general. In the course of trying to understand simulations of tidally locked lava planets, we found that there was not a full understanding of key features of their circulation. I explain how I used a two-dimensional model to represent the atmosphere of a tidally locked planet, and demonstrated that the equatorial jet that forms affects the global circulation and temperature pattern. This was key to our work on lava planets, but was applicable to any tidally locked planet.

Chapter 3 follows Chapter 2

In Chapter 3, I introduce the model I used to simulate three-dimensional planetary atmospheres, the General Circulation Model (GCM) Exo-FMS. Developing this model formed a large part of the work of my DPhil. I discuss the structure I developed, and the physical processes represented within it. I focus on the particular challenges of simulating tidally locked lava planets, and defer many technical details to Appendix A.

In Chapter 4, I discuss my first project using the simulations discussed in Chapter 3, to interpret observations of a lava planet.

Chapter 5 follows Chapter 4, and shows how in collaboration with Graham Lee we simulated dynamic, radiatively active clouds on 55 Cancri e in order to answer the questions raised by Chapter 4 on the effect of clouds in its atmosphere.

In the Conclusion, I summarise my work on the global circulation of tidally locked planets, and its relevance for 55 Cancri e.

CHAPTER 9

Conclusions

Bibliography

- Boyd, J.P. The Effects of Latitudinal Shear on Equatorial Waves. Part I: Theory and Methods. *Journal of Atmospheric Sciences*, 35(1):2236–2258, Dec. 1978.
- Boyd, J.P. *Chebyshev & Fourier Spectral Methods*. Springer, 2000.
- Demory, B.O. et al. Detection of a transit of the super-Earth 55Cancrie with warm Spitzer. *Astronomy & Astrophysics*, 533:A114, Sept. 2011.
- Demory, B.O. et al. A map of the large day–night temperature gradient of a super-Earth exoplanet. *Nature*, 532(7598):207–209, Mar. 2016.
- Hammond, M. and Pierrehumbert, R.T. Wave-Mean Flow Interactions in the Atmospheric Circulation of Tidally Locked Planets. *The Astrophysical Journal*, 869(1):65, Dec. 2018.
- Heng, K. and Workman, J. Analytical models of exoplanetary atmospheres. I. Atmospheric dynamics via the shallow water system. *Astrophysical Journal, Supplement Series*, 213(2):27, Aug. 2014.
- Iga, S.I. and Matsuda, Y. Shear Instability in a Shallow Water Model with Implications for the Venus Atmosphere. *Journal of Atmospheric Sciences*, 62(7):2514–2527, July 2005.
- Matsuno, T. Quasi-Geostrophic Motions in the Equatorial Area. *Journal of the Meteorological Society of Japan Ser II*, 44(1):25–43, 1966.
- Pierrehumbert, R.T. and Hammond, M. Atmospheric circulation of tide-locked exoplanets. *Annual Reviews, Submitted*, 2018.
- Shell, K.M. and Held, I.M. Abrupt Transition to Strong Superrotation in an Axisymmetric Model of the Upper Troposphere. *Journal of Atmospheric Sciences*, 61(2):2928–2935, Dec. 2004.

Bibliography

- Showman, A.P. and Polvani, L.M. The Matsuno-Gill model and equatorial superrotation. *Geophysical Research Letters*, 37(1):L18811–n/a, Sept. 2010.
- Showman, A.P. and Polvani, L.M. Equatorial Superrotation on Tidally Locked Exoplanets. *The Astrophysical Journal*, 738(1):71, Sept. 2011.
- Thuburn, J. and Lagneau, V. Eulerian Mean, Contour Integral, and Finite-Amplitude Wave Activity Diagnostics Applied to a Single-Layer Model of the Winter Stratosphere. *Journal of Atmospheric Sciences*, 56(5):689–710, Mar. 1999.
- Tsai, S.M., Dobbs-Dixon, I. and Gu, P.G. Three-dimensional structures of equatorial waves and the resulting super-rotation in the atmosphere of a tidally locked hot Jupiter. *Astrophysical Journal*, 793(2):141, Oct. 2014.
- Vallis, G.K. Atmospheric and Oceanic Fluid Dynamics. *Atmospheric and Oceanic Fluid Dynamics*, pages 770–, Nov. 2006.
- Winn, J.N. et al. A Super-Earth Transiting a Naked-Eye Star . *The Astrophysical Journal*, 737(1):L18, Aug. 2011.

APPENDIX A

Exo-FMS

Three-dimensional simulations are an important tool for understanding atmospheric dynamics and climate.

A General Circulation Model (GCM)

This chapter describes my work on the GCM Exo-FMS, and discusses the specific needs and issues of the atmospheres that I simulated with it.

I will discuss the dynamical core and grid of the model

This chapter does not include much scientific investigation, but I will try to show that an exoplanet GCM is not a fanciful attempt to recreate an unknowable planet, but can be used carefully alongside basic theories and real observations to understand processes that are only apparent in a full 3D representation of the planetary atmosphere. I will also argue that XX.

A.1 Model Structure

GFDL-FMS

Exo-FMS is based on the cubed-sphere dynamical core of the GFDL FMS.

Github Repository

It was very important that Exo-FMS should be openly available. I manage its Github repository and wiki.

ExoFMS Interface

Exo-FMS is meant to make the fewest modifications to the original FMS structure and cubed-sphere dynamical core as possible. To this end, I wrote a single interface to couple the dynamical core to our physics modules (radiative transfer, convection etc.).

A.2 Dynamics

The dynamical core of the GFDL-FMS solves the primitive equations.

For the work in Chapter 6, I used a dynamical core with a latitude-longitude grid. This grid was divided up by latitude, with each processors handling a certain number of latitude bands (three by default).

We found that the latitude-longitude grid did not deal well with instabilities at the poles of our simulations, particularly the very hot, tidally locked atmospheres under investiga-

tion. On a latitude-longitude grid, the cells get smaller and less stable towards the pole, and schemes are required to deal with cross-polar transport and instabilities. This led to the model unpredictably crashing without a particular cause.

To solve this problem, I updated the model to use a cubed-sphere grid.

A cubed-sphere grid is X.

As the version of the overall FMS system was newer for the new cubed-sphere dynamical core, it was simpler to just start again and treat it as a new model.

A.3 Radiative Transfer

I used a semi-grey radiative transfer scheme.

A.4 Cloud Microphysics

APPENDIX B

GFDL-SDC

The Spectral Dynamical Core.

APPENDIX C

Pseudo-Spectral Methods

In this appendix, we discuss how we solved the linearized shallow-water equations using a pseudo-spectral collocation method (Boyd, 2000). Defining a linear ordinary differential equation or system of equations:

$$Lu = q \quad (\text{C.1})$$

L is a differential operator acting on the variable u , and q is the forcing or eigenvalue term. The solution is written as a sum of a series of basis functions:

$$u(x) = \sum a_n \psi_n(x) \quad (\text{C.2})$$

For a system of equations rather than a single equation, L is a matrix and u and q are vectors. We impose the condition that the differential equation is satisfied at N “collocation points”, the positions of which depend on the set of basis functions.

This is equivalent to specifying that the “residual” – the difference between the exact solution and the pseudo-spectral series solution – is zero at these points. This provides N equations to solve for the N unknowns a_n , which gives the matrix equation:

$$\mathbf{H}\mathbf{a} = \mathbf{f} \quad (\text{C.3})$$

C.1 Solving Equations

Solving One Equation

[Boyd \(1978\)](#) solves the linearized shallow-water equations, by reducing them to a single equation for a single variable, and applying the pseudo-spectral method. In this paper, we solve the entire system of shallow-water equations at once with the method in Appendix C.1, but explain the method for a single equation here as it naturally leads to the second method ([Boyd, 2000](#)).

The matrix elements H_{ij} in equation C.3 are evaluated using the operator L at the collocation points x_i and for every mode ϕ_j , and the vector elements f_i are the terms q evaluated at the collocation points x_i :

$$H_{ij} = L\phi_j(x_i) \quad (\text{C.4})$$

$$f_i = q(x_i) \quad (\text{C.5})$$

This is then solved using a standard linear algebra routine to find a_n , and the solution

$u(x)$ is reconstructed using Equation C.2.

Solving Systems of Equations

The pseudo-spectral method can also be applied to systems of linear ordinary differential equations. For a system of forced, time-independent equations:

$$\mathbf{Lu} = \mathbf{q} \quad (\text{C.6})$$

The condition that the differential equation is satisfied at the collocation points gives the equivalent matrix equation to Equation C.3:

$$\mathbf{Ha} = \mathbf{f} \quad (\text{C.7})$$

\mathbf{H} is an $M \times N$ square matrix with elements:

$$H_{ij}^{kl} = L^{kl} \phi_j(x_i) \quad (\text{C.8})$$

i.e. the operator L^{kl} which acts on the l th variable in the k th equation, applied to the j th basis function and evaluated at the i th collocation point. \mathbf{f} is a vector made up of N subvectors f_i , which are the forcing terms in each equation evaluated at each collocation point.

$$\mathbf{H} = \begin{pmatrix} (H_{ij} & \dots)^{kl} & \dots \\ \vdots & \ddots & \dots \\ \vdots & & \ddots \end{pmatrix} \begin{pmatrix} (\alpha_i) \\ \vdots \\ \vdots \end{pmatrix} = \begin{pmatrix} (f_i) \\ \vdots \\ \vdots \end{pmatrix} \quad (\text{C.9})$$

\mathbf{H} is the same as the matrix in Equation C.4 with the elements H_{ij} replaced by sub-matrices H_{ij}^{kl} . Solving this system returns the coefficients of the basis functions, and the solutions are:

$$u(y) = \sum_{n=0}^N a_n \phi_n; \quad v(y) = \sum_{n=0}^N b_n \phi_n; \quad h(y) = \sum_{n=0}^N c_n \phi_n \quad (\text{C.10})$$

This gives a linear matrix equation with one solution corresponding to the coefficient vectors a_n, b_n, c_n of the forced solution.

Without forcing, the shallow-water equations define an eigensystem where the eigenvalue is the frequency ω .

$$\mathbf{L}\mathbf{u} = \omega \mathbf{P}\mathbf{u} \quad (\text{C.11})$$

The pseudo-spectral equation is then:

$$\mathbf{H}\mathbf{a} = \omega \mathbf{R}\mathbf{a} \quad (\text{C.12})$$

\mathbf{R} is an $M \times N$ square matrix with elements:

$$R_{ij}^{kl} = P^{kl} \phi_j(x_i) \quad (\text{C.13})$$

i.e. the eigenvalue operator P^{kl} acting on the l th variable in the k th equation, applied to the j th basis function and evaluated at the i th collocation point.

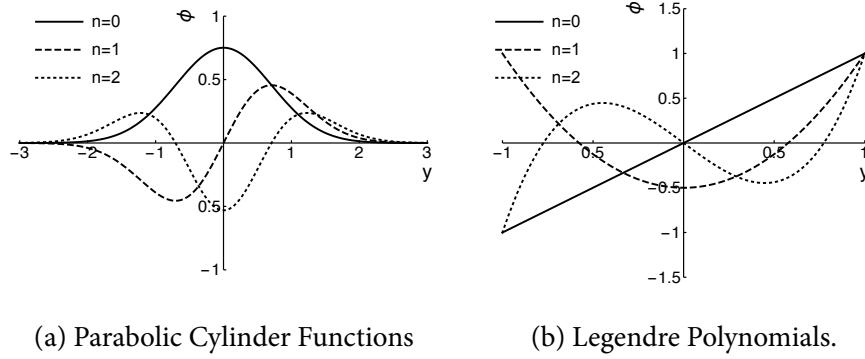


Figure C.1: Basis functions used in beta-plane and spherical coordinates.

$$\mathbf{H} = \left(\begin{pmatrix} H_{ij} & \dots \\ \vdots & \ddots \\ \vdots & \ddots \end{pmatrix}^{kl} \dots \right) \begin{pmatrix} \alpha_i \\ \vdots \\ \vdots \end{pmatrix} = \omega \left(\begin{pmatrix} R_{ij} & \dots \\ \vdots & \ddots \\ \vdots & \ddots \end{pmatrix}^{kl} \dots \right) \begin{pmatrix} \alpha_i \\ \vdots \\ \vdots \end{pmatrix} \quad (\text{C.14})$$

This gives an eigenvalue matrix equation, with N eigenvalues and eigenvectors, corresponding to the frequencies and coefficient vectors a_n , b_n , c_n for each free mode. Not all N modes must be physically realistic, so we identify the spurious modes by inspecting the eigenvalues for different values of N .

C.2 Example Solutions

Beta-plane solutions

We use the **parabolic cylinder functions** $\psi_n(y)$ ([Showman and Polvani, 2011](#)) as defined in Equation C.15 as a basis set for the pseudo-spectral method on the beta-plane (Equation ??), as they are the exact free solutions of [Matsuno \(1966\)](#) ([Boyd, 2000](#)).

Their collocation points are at their zeros (which are just the zeros of the Hermite polynomials H_n). Figure C.1a shows the first few **parabolic cylinder functions**.

$$\psi_n(y) = e^{-y^2/2} H_n(y) \quad (\text{C.15})$$

Figure C.2 shows the magnitude of the coefficients (Equation C.10) of the pseudo-spectral solution of the shallow-water equations linearized about a jet on a beta-plane (plotted in Figure ??). The first plot shows that when the background jet flow is zero, only modes up to $n = 2$ are non-zero. This is the analytic solution from [Matsuno \(1966\)](#), which the pseudo-spectral method identifies because we have used the free modes (the **parabolic cylinder functions**) as our basis functions.

For non-zero jet speed (corresponding to Figure ??), the pseudo-spectral series solution does not terminate, but the coefficients for the 30th mode are about eight orders of magnitude smaller than the largest mode. The beta-plane solutions in this paper were all calculated with at least 30 modes.

Spherical solutions

We use the Legendre polynomials as a basis set for the pseudo-spectral method in a spherical geometry (Equation ??). Figure C.1b shows the first few Legendre polynomials. Our collocation points are the zeros of these functions.

As discussed in Section ??, Equation ?? has a singularity at the poles, which we avoided by using a rescaled height γ , where $\gamma = h/\cos\phi$ ([Iga and Matsuda, 2005](#)). We replaced h with $\gamma \cos\phi$ in Equation ??, solved as normal, then multiplied the solution for

C.2. Example Solutions

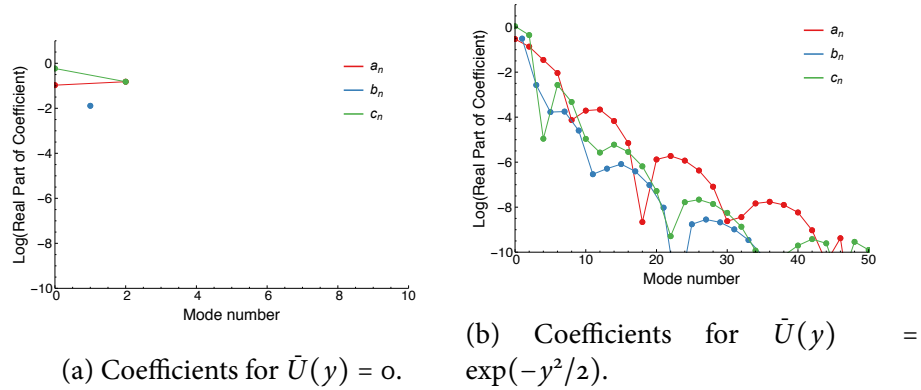
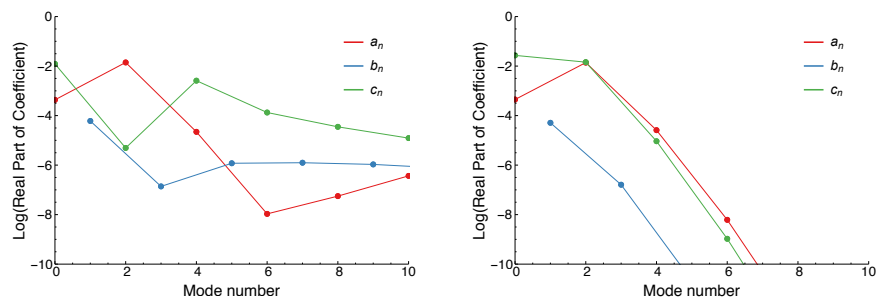


Figure C.2: Coefficients of the pseudo-spectral solution on the beta-plane coordinates with and without a background jet (the plots in Figure ??). The method identifies the exact solution in the first case, and converges rapidly to an accurate solution in the second case.

γ by $\cos \phi$ to recover the solution for h .

Figure C.3 shows how rescaling the h variable made the solutions converge much more quickly. In fact, the solutions without a rescaled h variable never reached a smooth solution at the poles.

C.2. Example Solutions



(a) Coefficients calculated with height h . (b) Coefficients calculated with rescaled height $y = h/\cos \phi$.

Figure C.3: Coefficients of the pseudo-spectral solution in spherical coordinates (the first plot in Figure ??), with the height variable h and the rescaled height y . Rescaling the height makes the method converge to a smooth solution at the poles.